Low Temperature Physics/Fizika Nizkikh Temperatur, 2015, v. 41, No. 4, pp. 315–337

Effects of anharmonicity of current-phase relation in Josephson junctions

(Review Article)

I.N. Askerzade

Computer Engineering Department and Center of Excellence of Superconductivity Research of Turkey, Ankara University, Ankara 06100, Turkey

Institute of Physics of Azerbaijan National Academy of Sciences, Baku Az-1143, Azerbaijan
E-mail: Iman.Askerzade@science.ankara.edu.tr

Received September 18, 2014, published online February 23, 2015

The aim of this review is the analysis of dynamical properties of Josephson junctions (JJ) with anharmonic current-phase relation (CPR). Firstly, discussion of theoretical foundation of anharmonic CPR in different Josephson structures and their experimental observation are presented. The influence of anisotropy and multiband effects on CPR of JJ are analyzed. We present recent theoretical study results of the anharmonic CPR influence on *I–V* curve, plasma frequency, and dynamics of long JJ. Results of study of Shapiro steps in *I–V* curve of anharmonic JJ are also presented. Finally, CPR anharmonicity effect on characteristics of JJ-based qubits is discussed.

PACS: **74.50.+r** Tunneling phenomena; Josephson effects;
03.67.-a Quantum information;
85.25.Cp Josephson devices;

Keywords: Josephson junction, two-band superconductors, qubits, current-phase relation, anharmonicity.

Contents

1. Introduction

The Josephson effect was discovered by Brian Josephson [1]. The stationary Josephson effect was first observed experimentally by Rowell [2], and the nonstationary Josephson effect was observed by Yanson et al. [3]. Since that time, there has been a continuously growing interest in the fundamental physics and applications of this effect. The achievements in Josephson-junction (JJ) technology have made it possible to develop a variety of sensors for detecting ultralow magnetic fields and weak electromagnetic radiation; they have also enabled the fabrication, testing, and application of ultrafast digital rapid single flux quantum (RSFQ) circuits as well as the design of large-scale integrated circuits for signal processing and general purpose computing [4,5].

It is clear that the Josephson effect, the 50th anniversary of which was celebrated in 2012, remains one of the most spectacular manifestations of quantum mechanics in all of experimental science. At its most fundamental level the Josephson effect is nothing more than the electronic analogue of interference phenomena in optical physics. But from this humble premise springs a huge range of physical phenomena and electronics applications which placed Josephson devices at the heart of physics research during the second half of the century of superconductivity and beyond.

The Josephson effect may be observed in a variety of structures. To realize such structures it is enough to fabricate a "weak" place interrupting the supercurrent flow in a superconductor or suppress the ability of a superconductor to carry a current, e.g., by deposition of a normal metal on its top, by implantation of impurities within a restricted volume, or by changing the sample geometry. One main characteristic of a JJ is the current-phase relation (CPR). Only in few cases CPR reduces to classical sinusoidal form with critical current I_c [6,7]:

$$I_S(\phi) = I_c \sin\phi. \tag{1}$$

Modern aspects of the supercurrent I_S dependence on the phase difference ϕ and the forms this dependence takes in Josephson junctions of different types (superconductor–normal–superconductor, superconductor–insulator–superconductor, double barrier, superconductor–ferromagnet–superconductor, superconductor–two-dimensional electron gas–superconductor junctions, and superconductor–constriction–superconductor point contacts) were discussed in [8,9]. CPR manifestations related to unconventional symmetry in the order parameters of a high-T_c superconductors were also widely investigated during last years [10–13]. As it follows from reviews [8–12] supercurrent I_S dependence on the phase difference ϕ can be presented in general as

$$I_S(\phi) = \sum_{n\geq 1}(I_c \sin n\phi + J_n \cos n\phi). \tag{2}$$

The shape of supercurrent $I_S(\phi)$ does not only depend on temperature and the distance between electrodes, but also on the critical temperature and transport parameters of both superconductors and the interface layer in JJ structures. Detailed analysis of CPR in different JJ structures was carried out in [9]. The pairing symmetry in superconducting state also strongly influences on CPR [11].

Simple sinusoidal form of CPR (1) was widely used to study the dynamics and ultimate performance of analogous and digital devices based on JJ up to recent time [4–14]. Above mentioned reviews [8–12] have been devoted to theoretical basis for the study of CPR in different Josephson structures. Results of these studies reveal fundamental physical mechanisms for control and experimental investigation of CPR. It is clear that modification of CPR in different JJ structures leads to changing of dynamical properties of Josephson circuits. Several recent research papers (see below) have been devoted to study dynamical effects in JJ with anharmonic CPR. Recent progress in the theoretical study and experimental investigation of dynamical properties of such junctions justifies an overview of the fundamentals of JJ dynamics with anharmonic CPR.

The main emphasis of this review is the investigation of CPR influence on dynamical properties of Josephson junctions. Firstly, we will briefly discuss influence of anisotropy and multiband effects of the order parameter in superconducting electrodes on the shape of CPR of JJ. The experimental investigations results concerning Josephson structures with anharmonic CPR are also reviewed. In second section we present detailed results of study of anharmonic CPR influence on *I–V* curve and on the plasma frequency of JJ. This section contains study of Shapiro steps in anharmonic JJ. Properties of long JJ with anharmonic CPR are also described in this section. Third section is devoted to detailed investigation of anharmonicity effects on characteristics of JJ qubits. Finally, conclusions are presented.

2. Influence of anisotropy and multiband effects of superconducting state on the CPR of JJ

2.1. JJ based on d-wave superconductors

For the calculation of Josephson current in such structures it is easy to use a Ginzburg–Landau theory of *d*-wave superconducting state based on its symmetry properties. Figure 1 presents schematic diagram of a JJ between pure $d_{x^2-y^2}$ superconductors. The gap states are assumed to align with the crystalline axes, which are rotated on angles θ_L and θ_R with respect to the junction normals $\mathbf{n}_L$ and $\mathbf{n}_R$ on the left and right-hand sides, respectively. It is well known that *d*-wave order parameter symmetry was observed in cuprate superconductors [10–12]. In this symmetry, we use a complex order parameter, which behaves the same way as the pair wave function [10]

$$\psi(\mathbf{k}) = \cos k_x - \cos k_y\,. \tag{3}$$

The Ginzburg–Landau free-energy functional F for *d*-wave superconductors has a form [15]

$$F = \int dV\,[A(T)\psi^2 + \beta\psi^4 + K_1(|D_x\psi|^2 + |D_y\psi|^2) + K_2|D_z\psi|^2 + \frac{1}{8\pi}\mathbf{B}(\mathbf{B}-2\mathbf{H})]\,. \tag{4}$$

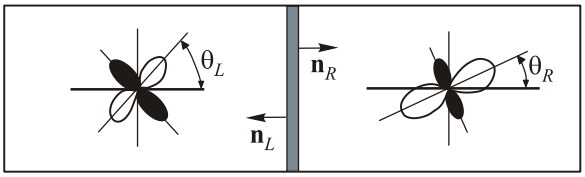

Fig. 1. Schematic diagram of a JJ between *d*-wave superconductors.

The real coefficients β and K_i are phenomenological parameters, and $A(T) = \gamma(T - T_c)$ changes its sign at the superconducting transition temperature T_c. The symbols D denote the components of the gauge-invariant gradient $D = [\nabla - (2\pi i\mathbf{A}/\Phi_0)]$, where $\mathbf{A}$ is the vector potential ($\mathbf{B} = \nabla \times \mathbf{A}$). For the calculation of the Josephson current, it is useful to introduce the coupling between the order parameters of two linked superconductors (Fig.1). Coupling between superconductors can be expressed through addition of term

$$F_{\text{coup}} = t \int dS \chi_1(\mathbf{n}_1)\chi_2(\mathbf{n}_2)\{\psi_1^*\psi_2 + \psi_2^*\psi_1\}, \qquad (5)$$

where t is a real parameter denoting the coupling strength. The functions $\chi_j(\mathbf{n}_j)$ are symmetry functions of the interface normal vector $\mathbf{n}_j$ in the crystal basis of the side j.
For the current density perpendicular to the interface we can get

$$I(\phi) = \frac{4\pi ct}{\Phi_0}\chi_1(\mathbf{n}_1)\chi_2(\mathbf{n}_2)|\psi_1||\psi_2|\sin\phi. \qquad (6)$$

For the d-wave superconductors usage of symmetry function as $\chi_1(\mathbf{n}_1) = n_x^2 - n_y^2$ [16] leads to final Sigrist–Rice result for clean JJ

$$I(\phi) = A_s \cos(2\theta_L)\cos(2\theta_R)\sin\phi, \qquad (7)$$

where A_s is a constant characteristic of the junction [12]. For the dirty limit of JJ the relation is:

$$I(\phi) = A_s \cos 2(\theta_L + \theta_R)\sin\phi. \qquad (8)$$

Basing a Green's function method the Josephson current in a d-wave superconductor/insulator/d-wave superconductor $(d/I/d)$ junction is calculated taking into account the anisotropy of the pair potentials explicitly [17,18]

$$R_N I(\phi) = \frac{\pi \bar{R}_N kT}{e}\left\{\sum_{\omega_n}\int_{-\pi/2}^{\pi/2}\left[\frac{a_1(\theta, i\omega_n, \phi)}{\Omega_{L,+}}|\Delta_L(\theta_+)| - \frac{\tilde{a}_1(\theta, i\omega_n, \phi)}{\Omega_{L,-}}|\Delta_L(\theta_-)|\right]\cos\theta d\theta\right\}, \qquad (9)$$

where $\Omega_{n,L,\pm} = \sqrt{\Delta_L^2(\theta_\pm) + \omega_n^2}$. The quantity R_N denotes the normal resistance and $\bar{R}_N$ is expressed as

$$\bar{R}_N^{-1} = \int_{-\pi/2}^{\pi/2} \sigma_N \cos\theta d\theta; \quad \sigma_N = \frac{4Z_0^2}{(1 - Z_0^2)\sinh^2(\lambda d_i) + 4Z_0^2\cosh(\lambda d_i)}, \qquad (10)$$

$$\lambda = \sqrt{1 - \kappa^2\cos^2\theta}\lambda_0; \quad Z_0 = \frac{\kappa\cos\theta}{\sqrt{1 - \kappa^2\cos^2\theta}}. \qquad (11)$$

Here, σ_N denotes the tunneling conductance for the injected quasiparticle when the junction is in the normal state. The quantity $\omega_n = 2\pi kT(n + 1/2)$ denotes the Matsubara frequency. The Andreev reflection [19] coefficient $a_1(\theta, i\omega_n, \phi)$ is obtained by solving the Bogoliubov equation [21], and $\tilde{a}_1(\theta, i\omega_n, \phi)$ is obtained substituting $\pi - \theta$, $-\phi_L$, and $-\phi_R$ for θ, ϕ_L, and ϕ_R into $a_1(\theta, i\omega_n, \phi)$, respectively. If we take only the $\theta = 0$ component, the magnitude of the Josephson current is proportional to $\cos(2\alpha)\cos(2\beta)$, and the phenomenological theory by Sigrist and Rice [16] is reproduced.

In general, supercurrent in JJ with d-wave superconductors $I(\phi)$ can be decomposed into the series of $\sin(n\phi)$ and $\cos(n\phi)$ using above presented Eq. (2). This equation includes the Josephson current component carried by the multiple Andreev reflection processes at the interface. In the above equation, the current components with index n correspond to the amplitudes of the $n$ths reflection processes of quasiparticles. For $\sigma_N \sim 0$, supercurrent $I(\phi)$ is proportional to $\sin(\phi)$ and the classical results of Ambreokar–Baratoff theory [22] are reproduced, while for $\sigma_N = 1$, above Eqs. (5)–(11) reproduce the previous results of Kulik and Omel'yanchuk theory [23,24]. On the other hand, for a fixed phase difference between two superconductors, the component of the Josephson critical current becomes either positive or negative depending on the injection angle of the quasiparticle (as it follows from Tanaka's analysis [17,19]). In some situations, the phase difference ϕ_0, which gives the free energy minima, is located at neither zero nor π. When the crystal axis is tilted from the interface normal, zero-energy states i.e. midgap states, are formed near the interface depending on the angle of the crystal axis and the injection angle of the quasiparticle. This effect leads to enhancement of the Josephson current at low temperatures.

Negative Josephson coupling was first noted by Kulik many years ago [3]. He discussed the spin-flip tunneling through an insulator with magnetic impurities. Late Bulaevskii *et al.* [20] proved that under some conditions such spin-flip tunneling prevails over the direct tunneling and leads to a π-junction. The junction energy achieves minimum at the phase difference $\pm\pi$, and a spontaneous supercurrent may appear in a circuit containing the junction. Two possible directions of the supercurrent reflect the doubly degenerated ground state. In contrast to the usual junction such a state is achieved without application of an external field.

2.2. JJ between two-band superconductors

Multiband superconductivity became a hot topic in condensed matter physics in 2001, when the two-band superconductivity in MgB_2 with anomalous high $T_c = 39\,\mathrm{K}$ was discovered [25]. It is striking that the pairing mechanism had electron-phonon origin in magnesium diboride and that order parameters, which are attributed to superconducting energy gaps, have *s*-wave symmetry. Iron-based superconductors, which have been discovered not long ago, and nonmagnetic borocarbides [15,26] can be classified as multiband systems. In this section the stationary Josephson effect in SCS (superconductor–constriction–superconductor) junction is presented. The behavior of such junctions even in the case of one-band superconductors, as revealed in [23,24], has the qualitative differences comparing to SIS (superconductor–insulator–superconductor) tunnel junctions. The microscopic theory of the "dirty" SCS junction for two-band superconductors is built, which generalizes the Kulik–Omel'yanchouk theory in this case [27]. The case of dirty two-band superconductor with strong intra-band scattering rates by impurities (dirty limit) and weak interband scattering is investigated [27]. In the dirty limit superconductor is described by the Usadel equations for normal and anomalous Green's functions *g* and *f*, which for two-band superconductor take the form presented in [27] (Fig. 2). Calculation of the Josephson current between two-band superconductors in the absence of inter-band scattering leads to:

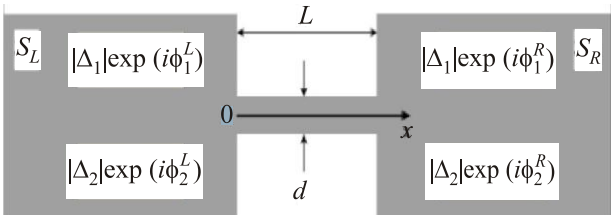

Fig. 2. Schematic diagram of a Josephson junction between two-band superconductors.

$$I(\phi) = \left\{ \frac{4\pi T}{eR_{N1}} \sum_{\omega>0} \frac{\Delta_1 \cos(\phi/2)}{\sqrt{\omega^2 + \Delta_1^2 \cos^2(\phi/2)}} \arctan \frac{\Delta_1 \sin(\phi/2)}{\sqrt{\omega^2 + \Delta_1^2 \cos^2(\phi/2)}} + \right.$$
$$\left. + \frac{4\pi T}{eR_{N2}} \sum_{\omega>0} \frac{\Delta_2 \cos(\phi/2)}{\sqrt{\omega^2 + \Delta_2^2 \cos^2(\phi/2)}} \arctan \frac{\Delta_2 \sin(\phi/2)}{\sqrt{\omega^2 + \Delta_2^2 \cos^2(\phi/2)}} \right\}. \tag{12}$$

As it follows from Eq. (12) current flows independently from the first band to the first one and from the second band to the second one. This equation is a straightforward generalization of Ambreokar-Baratoff results for one-band superconductor [22]. Introducing the total resistance $R_N = R_{N1}R_{N2}/(R_{N1} + R_{N2})$ and normalizing the current on the value $I_0 = (2\pi/eR_N)T_c$ the current-phase relations for different values of $r = R_{N1}/R_{N2}$ and temperature T are plotted in Fig. 3(a, b). Results of calculation of critical current temperature dependence for two-band based JJ are presented in Fig. 4. For the calculation of $I(\phi)$ and $I_c(T)$ the parameters for two-band superconductor MgB_2 without inter-band interaction [15,27] were used. The deformation of $I(\phi)$ curve depending on different parameters of JJ based on two-band superconductors is clear.

Using perturbation theory in the first approximation for Green's functions in each band for the case of nonzero interband scattering, the corrections to the current (12) $\delta I = \delta I_1 + \delta I_2$ were obtained [27]:

$$\delta I_1 = \frac{2\pi T \gamma_{12}}{eR_{N1}} \sum_{\omega} \left[\frac{\omega^2 (\Delta_2 e^{i\delta} - \Delta_1)\cos(\phi/2)}{\sqrt{(\omega^2 + \Delta_1^2 \cos^2(\phi/2))^3}\sqrt{\omega^2 + \Delta_2^2}} \arctan \frac{\Delta_1 \sin(\phi/2)}{\sqrt{\omega^2 + \Delta_1^2 \cos^2(\phi/2)}} + \right.$$
$$\left. + \frac{1}{2} \frac{\omega^2 (\Delta_2 e^{i\delta} - \Delta_1)\sin\phi}{(\omega^2 + \Delta_1^2)(\omega^2 + \Delta_1^2 \cos^2(\phi/2))\sqrt{\omega^2 + \Delta_2^2}} \right], \tag{13}$$

$$\delta I_2 = \frac{2\pi T \gamma_{12}}{eR_{N2}} \sum_{\omega} \left[\frac{\omega^2 (\Delta_1 e^{i\delta} - \Delta_2)\cos(\phi/2)}{\sqrt{(\omega^2 + \Delta_1^2 \cos^2(\phi/2))^3}\sqrt{\omega^2 + \Delta_2^2}} \arctan \frac{\Delta_2 \sin(\phi/2)}{\sqrt{\omega^2 + \Delta_2^2 \cos^2(\phi/2)}} + \right.$$
$$\left. + \frac{1}{2} \frac{\omega^2 (\Delta_1 e^{i\delta} - \Delta_2)\sin\phi}{(\omega^2 + \Delta_2^2)(\omega^2 + \Delta_2^2 \cos^2(\phi/2))\sqrt{\omega^2 + \Delta_1^2}} \right]. \tag{14}$$

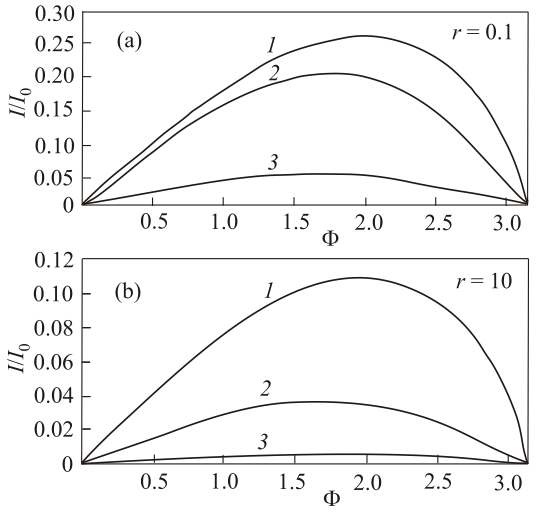

Fig. 3. CPR of MgB_2/MgB_2 junction for different temperatures T: 0(*1*); $0.5T_c$(*2*); $0.9T_c$(*3*) and ratios of resistances $r = R_{N1}/R_{N2}$.

where γ_{12} is parameter of the interband scattering, and δ is a phase shift. When the interband scattering is taken into account and the phase shift $\delta \neq 0$, the phases of Green's functions d_0 not coincide with phases of order parameters Δ_i. From the above-mentioned discussion it follows that CPR of JJ based on two-band superconductors also deviates from simple sinusoidal form (1) (see Fig. 3).

2.3. CPR relation of JJ structures with FM and AFM layers

In this part we pay attention to the approach based on the Usadel equation and consider the S/F/S junction with F layer of thickness $2d_f$ (Fig. 5). The following formula for the supercurrent was used in [8,28]

$$I(\phi) = ieN(0)D_f \pi TS \sum_{-\infty}^{\infty} \left(F\frac{d\tilde{F}}{dx} - \tilde{F}\frac{dF}{dx} \right), \qquad (15)$$

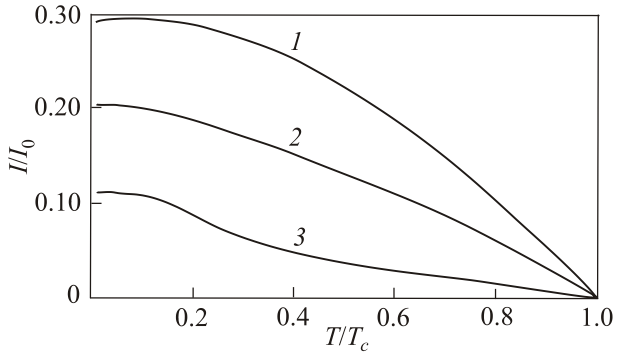

Fig. 4. Temperature dependencies of critical current I_c for different values of $r = R_{N1}/R_{N2}$: 0.1(*1*); 1(*2*); 10(*3*).

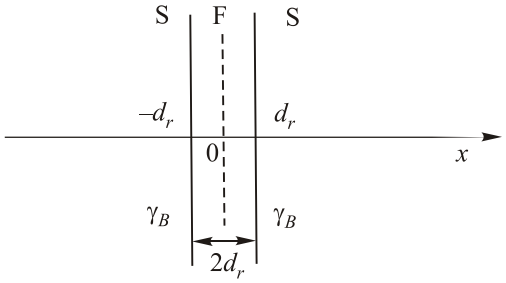

Fig. 5. Schematic description of *S*/*F*/*S* junction.

where anomalous Green's function $F(x)$ depends only on one coordinate x, and this function meets following conditions:

$$\tilde{F}(x,h) = F^*(x,-h) : F_s(-d_f) = \frac{\Delta e^{-i\phi/2}}{\sqrt{\Delta^2+\omega^2}},$$

$$F_s(d_f) = \frac{\Delta e^{-\phi/2}}{\sqrt{\Delta^2+\omega^2}},$$

S is the junction cross-section area, and $N(0)$ is the electron density of state for one-spin projection. The last expression gives the usual sinusoidal current-phase dependence with the critical current [28]:

$$I_c = eN(0)D_f \pi TS \sum_{-\infty}^{\infty} \left(\frac{\Delta^2}{\omega^2} \frac{2k/\cosh(2kd_f)}{\tanh(2kd_f)(1+\Gamma_\omega^2 k^2) + 2k\Gamma_\omega} \right), \qquad (16)$$

where $\Gamma_\omega = \gamma_B \xi_N / G_s$. Generalization of the presented theory on the case of the different interface transparencies is presented in [9,29]. It gives:

$$I_c = \frac{V_0}{R_N} 4y \frac{\cos 2y \sinh(2y) + \sin 2y \cosh(2y)}{\cosh(4y) - \cos 4y}, \qquad (17)$$

where $y = (d_F/\xi_F)\sqrt{H/(2\pi T_c)}$, H is the exchange energy in F layer. The S/F/S junctions reveal the nonmonotonic behavior of the critical current as a function of the F layer thickness. Vanishing of the critical current signals the transition from the state 0 to the state π. It occurs at $2y_c = 2.36$ which is exactly the critical value of the F layer thickness in the S/F/S multilayer system corresponding to the 0–π-state transition (Fig. 6) [8,9].

CPR in different structures such as SFcFS and double-barrier SIFIS are presented in [30], where the nonmonotonic temperature dependence of the critical current is analyzed. Deformation of CPR of double-barrier SIFIS junctions for different exchange integrals in F layer is presented in Fig. 7. Similar change in CPR was experimentally observed in [31]. One of the interesting properties of SFS systems is the rotation of the magnetization vector of F layer under action of an external magnetic field [32–34]. Details of CPR of different Josephson structures with F

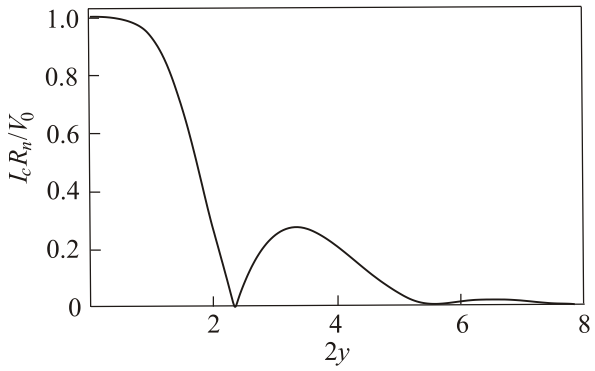

Fig. 6. Critical current of S/F/S junctions versus $y = d_F/\xi_F\sqrt{H/(2\pi T_c)}$, where H is the exchange energy.

layer were presented in excellent reviews [8,9]. The study of the CPR is also important for understanding the fundamental properties of superconducting materials, such as symmetry of the superconducting correlation and peculiarities of the spin transport in multilayer systems based on superconducting and ferromagnetic materials.

Despite wide discussion about JJ with FM layers, there are few papers concerning investigations of structures with AFM layers. Firstly such structure was studied by Gor'kov and Kresin [35]. They found that the critical current strongly depends on external magnetic field. The analytical expression can be written as

$$I_c(M_s) = I_{c0}\sqrt{\frac{2}{\pi\gamma M_s}}\cos\left(\beta M_s - \frac{\pi}{4}\right), \qquad (18)$$

where $\gamma >> 1$ is related to characteristic of AFM layer, $0 < M_s < 1$ is parameter of AFM ordering, I_{c0} is critical current in the absence of external magnetic field coinciding with corresponding critical current in SNS junctions. It is useful to note the importance of study of JJ with magnetically ordered layers. As mentioned in [5], such Josephson structures may allow substantial savings in the Josephson circuit area.

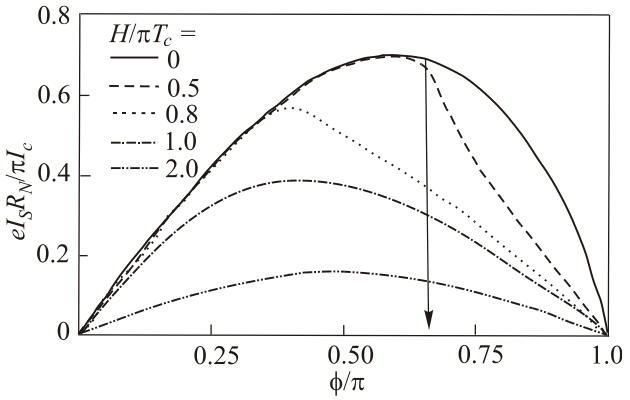

Fig. 7. Deformation of CPR of SIFIS junction for different exchange energies.

2.4. Experimental results of CPR investigations in different Josephson structures

As it follows from above presented theoretical review, the general case CPR in Josephson structures is determined by the types of JJ. At high temperatures $(T_c - T << T_c)$ deviation of CPR $I(\phi)$ from $\sin\phi$ law is negligible for any type of JJ. At low temperatures $(T << T_c)$ the relation $I(\phi) = \sin\phi$ takes place for SIS junctions [36]. In early investigations [36], the high accuracy realization of sinusoidal character of CPR was shown using plasma resonance technique. Recently, Gronbech-Jensen *et al.* [37] studied the dynamics of the tunnel JJ simultaneously carrying dc and ac currents by measuring the statistics of switching of low-temperature Nb–$NbAlO_x$–Nb type tunnel junctions to the resistive state. The critical current statistics in this system, which is controlled by thermal fluctuations at the bottom of the potential well $U(\phi) = E_J(-i\phi + 1 - \cos\phi)$, was determined for 10000 events. By changing the amplitude of ac current, it was possible to control the dc current corresponding to a peak in the switching events distribution.

A new method for CPR measurement and some of its practical applications were presented in [38,39]. Most commonly for the experimental investigation of the CPR, the weak link of interest is incorporated in a superconducting ring with a sufficiently small inductance L. This circuit is usually called a single-junction interferometer [4]. Under limitations $\omega L/R_N << 1$, and $\omega^2 LC << 1$ the superconducting part $I_s(\phi) = I_c f(\phi)$ of the current exceeds essentially all other components, so the following equation is valid for single junction interferometer [38,39]:

$$\phi = \phi_e - lf(\phi), \qquad (19)$$

where l is the normalized inductance, $l = 2\pi LI_c/\Phi_0$. There is a more precise method to determine the CPR using radio frequency (rf) technique. It was proposed many years ago [40,41]. Further development of this method was presented

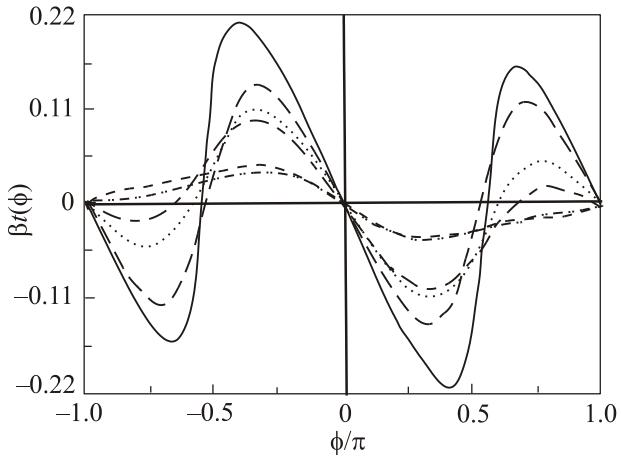

Fig. 8. Experimental CPR of symmetric $\pi/4$ grain-boundary junction.

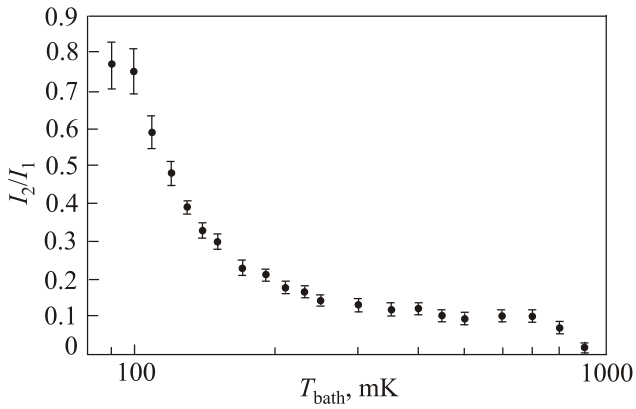

Fig. 9. YBCO based grain boundary junction: I_2/I_1 versus temperature.

by Ii'ichev *et al*. in [42]. They have shown that the CPR and the phase-dependent conductance can be extracted from experimental data. Results of measurements of Josephson current through a junction as a function of the phase difference ϕ in symmetric 45° grain-boundary high-T_c junction are presented in Fig. 8 [43]. Recent achievements in fabrication of the JJ based on high-T_c superconductors were described in [44]. Measurements reveal that YBCO-based grain boundary tunnel junctions fabricated in [44] are highly hysteretic and Fig. 9 shows the ratio of coefficients I_1 and I_2 determined by a Fourier analysis of the CPR at various temperatures. With decreasing T, value of I_2 grows monotonically down to $T = 4.2\,\mathrm{K}$, while the I_1 component exhibits only a weak temperature dependence [44]. Very recent review of physical properties of JJ based on high-T_c superconductor was presented in [45]. Furthermore anharmonic CPR in graphene JJ was reported recently in experimental research [46] and corresponding theoretical calculations were proposed in [47].

Very recently, topological insulators attached to superconductors have attracted great interest of researchers. The topological insulator offers a new state of matter, which is topologically different from the conventional band insulator [48–50]. When SF junctions are deposited on a topological insulator, surface Dirac fermions gain a domain wall structure of the mass. The CPR shows 4π periodicity,

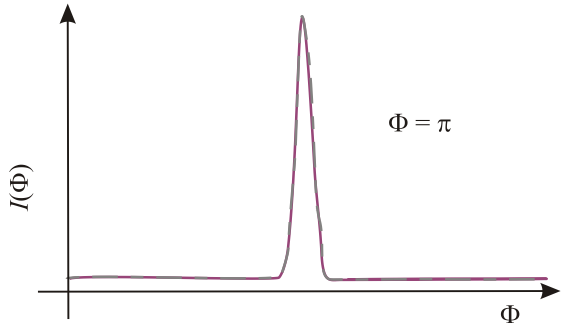

Fig. 10. CPR of superconductor-topological insulator junction.

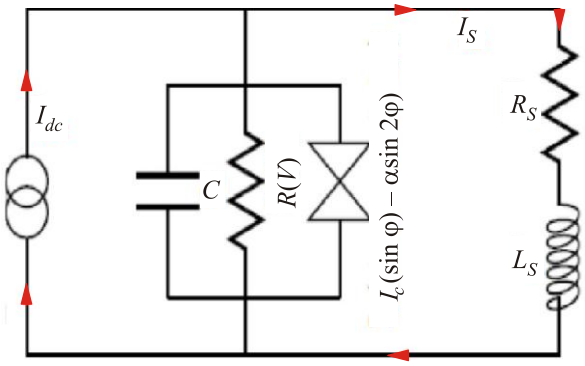

Fig. 11. Circuit model of RCLSJ.

i.e., the shape of supercurrent has a form of $\sin(\phi/2)$ [51,52]. JJ in hybrid superconductor-topological insulator devices revealing two peculiarities was reported in [53]. I_cR_N products for this structures is inversely proportional to the width of the junction. Another property is related to a low characteristic magnetic field needed for suppression of supercurrent, i.e., Fraunhofer capture is different from traditional dependence $I_c(H)$ [4]. The shape of CPR for such a junction is presented in Fig. 10. Detailed analysis of the superconductor-topological insulator junctions is the subject of future investigations.

3. Influence of anharmonic effects of CPR on JJ dynamics

3.1. Anharmonic effects in I–V curve

For a long period, the real shape of the CPR was not considered as an important factor affecting dynamical properties of JJ. Tunnel Josephson junction of SIS structure reveals $I_S(\phi) = \sin\phi$, which was observed experimentally with high precision for such junctions (see above). The shape of the CPR, or more explicitly the energy and phase dependencies of spectral current density have become important parameters in the analysis of the dynamic properties of Josephson junction circuits. Small deviation from harmonic case does not essentially affect the response of the junctions on a steady magnetic field and may be taken into account in the circuit design as an additional intrinsic inductance (see [54]), which must be added to the geometrical one in the circuit simulation. In this section, we study *I–V* curve of JJ with considerably anharmonic CPR using relation $I_J = I_c(\sin\phi - \alpha\sin 2\phi)$. The resistively, capacitively, inductively shunted Josephson junction (RCLSJ) circuit shown in Fig. 11 is shunted by a small external resistor isatisting $R_s \ll R_n$ [4,55,56]. Here R_n and R_s denote the normal state and shunt resistances, respectively. As shown in the Fig. 11 the Josephson tunnel junction is replaced by three parallel current channels. The total current through JJ is represented as a sum of the supercurrent $I(\phi)$, the displacement current $I_D = C(dV/dt)$, and the normal current due to quasiparticles

$I_N = V/R(V)$. The voltage-dependent junction resistance [4,55] is assumed to be:

$$R(V) = \begin{cases} R_n & \text{if } |V| > V_g, \\ R_{\text{sg}} & \text{if } |V| \le V_g. \end{cases} \tag{20}$$

where $V_g = 2\Delta/e$ is the gap voltage that depends on the energy gap (i.e., Δ) of superconductor, R_n is the normal state resistance and R_{sg} is the sub-gap resistance of the JJ in the superconducting state. The applied bias current I_{dc} is carried by the sum of the listed components (I_J, I_N, I_S). $I_J = I_c(\sin\phi - \alpha\sin 2\phi)$, $I_N = V/R(V)$, $I_D = C(dV/dt)$. $I = I_D + I_N + I_J + I_s$ where I_s denotes the current in the shunt branch. For simplicity, we ignore the effect of thermal noise throughout this study $(I_{\text{fluc}} = 0)$.

Equations that correspond to the circuit in Fig. 11 in dimensionless form are

$$\frac{d\phi}{d\tau} = v,$$

$$\beta_C \frac{dv}{d\tau} + g(v)v + f(\phi) + i_s = i, \tag{21}$$

$$\beta_L \frac{di_s}{d\tau} + i_s = v,$$

where $\beta_C = (2e/\hbar)I_c C R_s^2$ is the McCumber capacitance parameter; $g(v) = R_s/R(v)$ is the normalized tunnel junction conductance; $i_s = I_s/I_c$ is dimensionless shunt current; $i = I/I_c$ is dimensionless external dc bias current; $\beta_L = (2e/\hbar)I_c L_s$ is the dimensionless inductance; $\tau = \omega_c t$ is the normalized time, $\omega_c = (2e/\hbar)V_c$ is the characteristic frequency, and $V_c = I_c R_s$ is the characteristic voltage. The relationship between β_C and ω_c can be written as $\beta_C = (\omega_c/\Omega_p(0))^2$ where plasma frequency $\Omega_p(0) = \sqrt{2eI_c/\hbar C}$.

The solutions of Eqs. (21) are numerically obtained using MATLAB routine based on adaptive Runge–Kutta method [57]. The time-averaged voltage for the determination of *I–V* curve can be evaluated using the expression:

$$\langle v \rangle = \langle d\phi/d\tau \rangle = \frac{1}{\tau_{rng}} \int_0^{\tau_{rng}} v(\tau) d\tau, \tag{22}$$

where τ_{rng} is the sampling range. Note that τ_{rng} in Eq. (22) is taken much longer than the period of Josephson oscillations as well as relaxation oscillations. For that reason, the time-averaged voltage in Eq. (22) is sometimes called in literature as long-time averaged voltage.

In order to study the influence of second harmonic on the dynamics of the JJ, we firstly evaluated the critical current related to the amplitude of both harmonics. In such way, the normalized critical current can be found as an extremum of the function $f(\phi) = (\sin\phi - \alpha\sin 2\phi)$

$$I_c/I_{c_0} = \max(f(\phi)), \tag{23}$$

where I_{c_0} is the critical current at $\alpha = 0$. The normalized critical current with respect to anharmonicity parameter α is plotted in Fig. 12. As shown in the figure, I_c is nonlinear for small α, whereas it is linear for large α values. Moreover, the linear dependence of critical current I_c was experimentally observed at large α in YBCO-based JJ [43]. In addition, a similar plot in Fig. 12 was obtained using analytical expression for critical current given in [58].

Two types of dynamics of RCLSJ circuit presented in Fig. 13 can be explained using load-line analysis associated with *I–V* curve of the JJ. The first case is shown in Fig. 13(a) and corresponds to relaxation oscillations in the circuit with parameters $i = 1.1$, $\beta_{C_0} = 1.11$, $\beta_{L_0} = 21.7$ at $\alpha = 0$. Relaxation oscillations in Josephson circuits have been studied by many authors [55] and [59]. A similar relaxation generator was used to study the dynamical properties of tunnel JJ comparator in [60]. The second regime corresponds to the regular ac Josephson oscillations [55] and it is shown in Fig. 13(b) with parameters $i = 1.1$, $\beta_{C_0} = 2.22$, $\beta_{L_0} = 43.4$, at $\alpha = 0$. For nonzero anharmonicity parameter such as $\alpha = 0.4$ (see Fig. 13(c)), the amplitude of the Josephson oscillations becomes smaller, which is related to the effective capacitive properties of JJ. Such situations can be explained by the increase of the critical current of JJ with anharmonic CPR (the detailed discussion is given below).

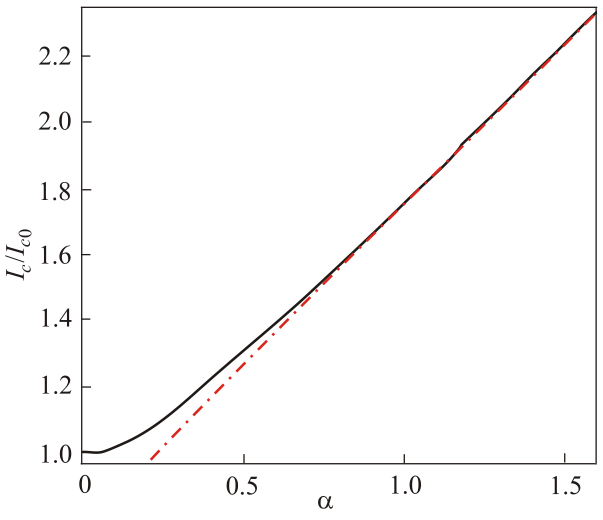

Fig. 12. (Color online) Normalized critical current versus anharmonicity parameter α.

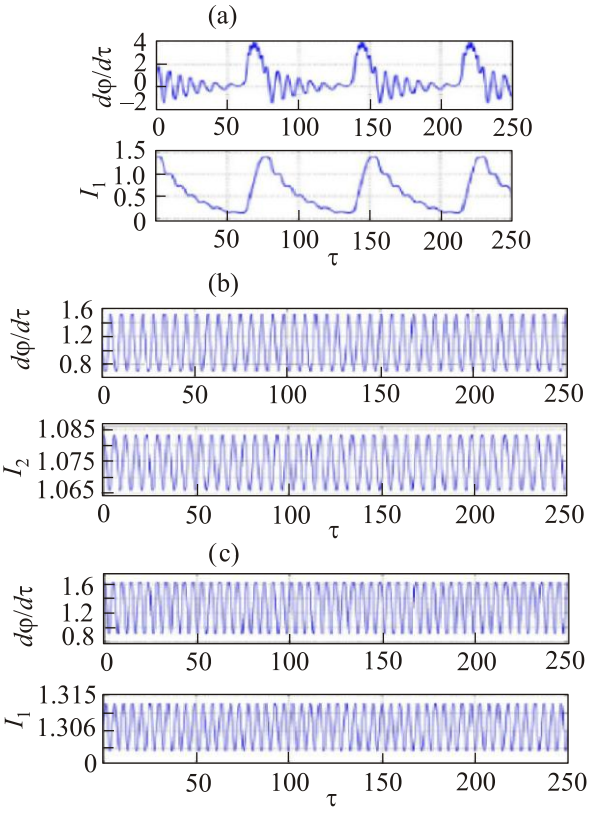

Fig. 13. (Color online) Time dependence of dynamical variables: voltage $d\varphi/d\tau$ and current I through shunt branch. Computational parameters are: $i = 1.1$, $\beta_{C0} = 1.11$, $\beta_{L0} = 21.7$, $\alpha = 0$ (a); $i = 1.1$, $\beta_{C0} = 2.22$, $\beta_{L0} = 43.4$, $\alpha = 0$ (b); $i = 1.336$, $\beta_{C0} = 2.696$, $\beta_{L0} = 52.701$, $\alpha = 0.4$ (c).

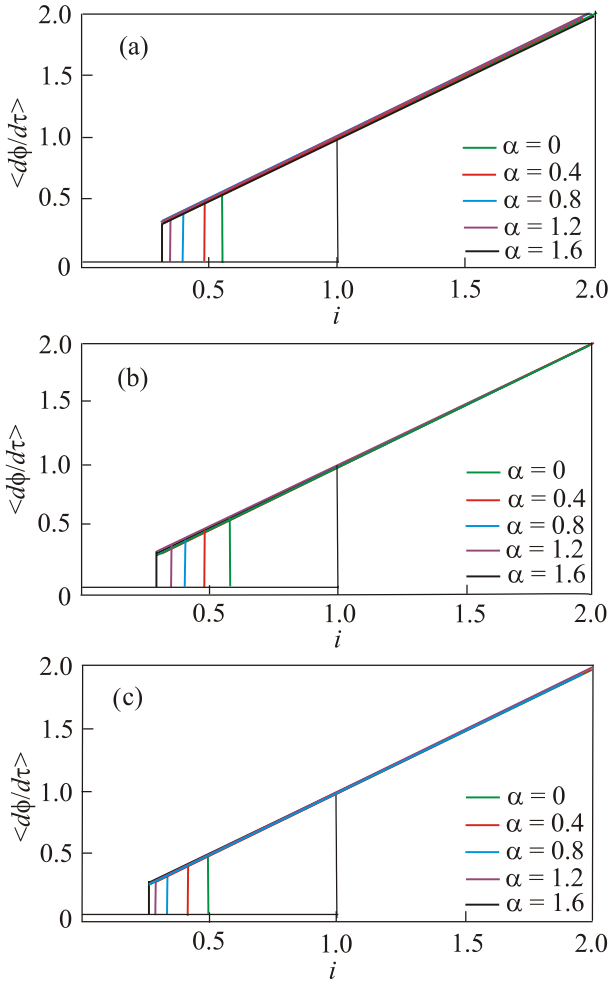

Fig. 14. (Color online) *I–V* curves for various α values at $\beta_{C0} = 10$; $\beta_{L0} = 1$ (a); $\beta_{L0} = 10$(b); $\beta_{L0} = 30$ (c).

In paper [57] numerical analysis of *I–V* characteristics for different α values was performed as shown in Fig. 14. In the figure, we have plotted *I–V* characteristics of the system with different β_{C_0} and β_{L_0} values using the same R_s, R_{sg}, and R_n from Table 1, similar [55]. Note that β_{C_0} and β_{L_0} refer to the harmonic case of the CPR (i.e., $\alpha = 0$). Similar results were obtained in [61] for $\alpha = 0.2$ case only due to the limited nature of the analytical calculations. Furthermore, it is difficult to study directly the details of the dynamics both experimentally and analytically, therefore, we can rely on numerical solutions of Eqs. (21) to study the influence of anharmonicity parameter α. As can be seen from Fig.14, the width of the hysteresis in the *I–V* curve becomes larger with an increase of anharmonicity parameter α. Consequently, the presence of anharmonic CPR impacts the inertial properties of the JJ as an undesirable effect. In addition, we repeat few simulations using opposite sign of the anharmonicity parameter α in relation to our calculations presented here. We observed that the hysteresis of the *I–V* characteristics decreases compared to its counter part in the presented plots. In general case, the sign of α is determined by the physical properties of barrier layer in Josephson structure [10,20,58].

Table 1. Fabrication parameters of Josephson junctions (see [55])

T, K	I_{c0}, mA	V_g, mV	R_{sg}, Ω	R_n, Ω	R, Ω
4.22	0.550	2.91	50	3	1.1
7.60	0.275	2.09	15	3	1.1

The size of hysteresis in *I–V* curve is characterized by the return current, at which the JJ switches from R-branch to S-branch in the *I–V* curve. The relationship between the return current and high values of McCumber parameter β_C can be obtained using simple resistive model [4]:

$$\frac{I_R}{I_c} = \frac{4}{\pi}\frac{1}{\sqrt{\beta_C}}. \qquad (24)$$

If we consider Eq. (20), the return current vs McCumber parameter qualitatively reveals a similar behavior [4]. The deviation from the expression in Eq. (24) becomes larger when the ratio of R_{sg}/R_n increases. On the other hand, the return current I_R is not only a function of

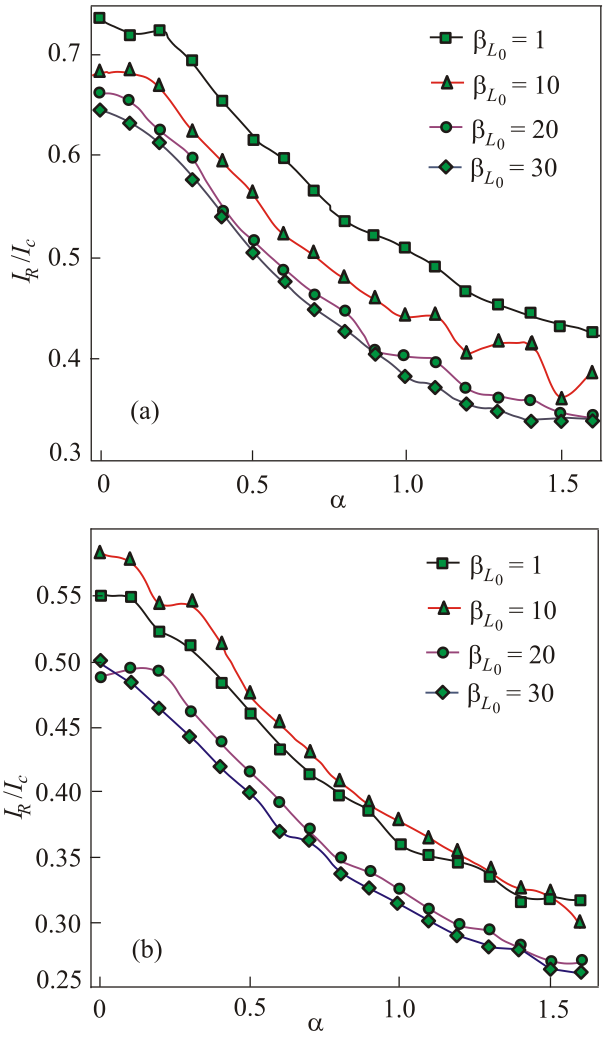

Fig 15. (Color online) Return current dependence on anharmonicity parameter α, at β_{C0}= 5 (a); β_{C0} = 10 (b).

β_C but also a function of α and β_L. However, it is difficult to obtain an explicit analytical expression for it. For this reason, numerical simulations are performed to analyze the influence of anharmonicity parameter α and dimensionless inductance β_L on the normalized return current I_R/I_c at two different values of McCumber parameter (e.g., $\beta_{C_0} = 5$ and $\beta_{C_0} = 10$).

First of all, we will discuss the relationship between I_R/I_c and α which is shown in Fig. 15 for various β_{L_0} values. In general, the influence of the capacitance and inductance of the JJ on the junction impedance is of opposite character. That is why one reactive element will damp the influence of the other. This implies that corresponding *I–V* curve and associated hysteresis will be determined by the resulting impedance. At fixed β_{L_0}, the value of the Josephson inductance $L_c = (\hbar/2e)/I_c$ decreases with α increasing. As a result, the influence of the junction capacitance at nonzero α on the *I–V* curve becomes dominant compared to harmonic case. If we compare the plots here with the results in [61], the normalized return current

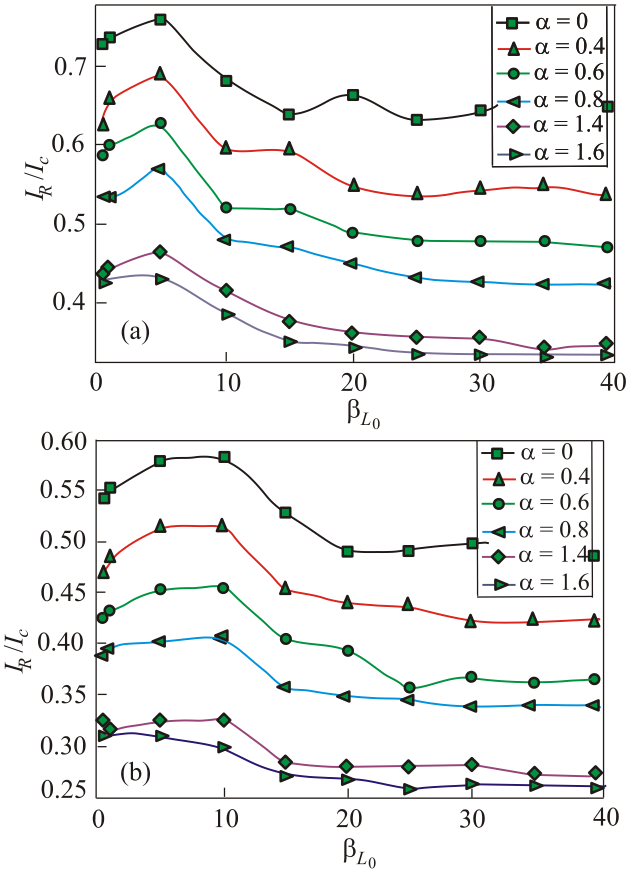

Fig. 16. (Color online) Return current dependence on dimensionless inductance β_{L0} at β_{C0}= 5 (a); β_{C0} = 10 (b).

I_R/I_c, is defined here accurately in contrast to the result therein. The reason is that the author in introduced [61] an approximate solution using analytical approach.

The exact value of return current is sensitive to the characteristics of the junction in the subgap region. Usually a switching from R-state to S-state leads to an exponential decay of the voltage transient waveform. As mentioned in [4], the voltage transient from R-state to S-state is accompanied by a slowly damped plasma oscillation. For this reason, we observed inaccuracies at some points on the curves presented in Fig. 15. The accuracy of our calculations for the return current in Fig. 15 was roughly estimated as 5%.

The relationship between return current I_R/I_c and dimensionless inductance β_L is illustrated in Fig. 16 for various α. The junction circuit shown in Fig. 11 is shunted by a serially connected inductance L_s and shunt resistor R_s. This means that the junction is shunted by impedance

$$\frac{Z_s}{R_s} = \sqrt{1+\left(\frac{\omega L_s}{R_s}\right)^2}. \qquad (25)$$

At vanishing shunt inductance (i.e., $\omega L_s \ll R_s \ll R_{sg}$), we come to standard resistively shunted junction (RSJ)

model with hysteresis on *I–V* curve controlled by McCumber parameter $\beta_C = (2e/\hbar)I_c CR_s^2$. With increasing inductance L_s the impedance Z_s also increases. On the other hand, if the shunting effect is in the high shunting inductance limit (i.e., $\omega L_s \gg R_s$) the impedance Z_s approaches ωL_s. In this case, the impedance Z_s becomes much greater than R_{sg} and R_n (i.e., $Z_s \gg R_{sg} \gg R_n$). As a result, McCumber parameter β_C can be determined by sub-gap resistance R_{sg}: $\beta_C(R_{sg}) = (2e/\hbar)I_c CR_{sg}^2$. Due to that reason, $\beta_C(R_{sg})$ will become greater than β_C. The return current I_R/I_c approximately reaches the constant values lower than corresponding value for $\omega L_s \ll R_s$. It is shown in Fig. 16, that the crossover from one regime to another reveals a peak character. Furthermore, as it follows from Fig. 16, peaks width increases for large McCumber parameter β_C. The inaccurate behavior similar to that in Fig. 16 is also observed on the curves in Fig. 15 due to the transient plasma oscillation in R → S switching.

3.2. Plasma frequency of JJ with anharmonic CPR

It is useful to discuss the influence of CPR anharmonicity on small perturbations of the S state of JJ, i.e., the possible phase motion in the vicinity of equilibrium state ϕ_0. It is known, that JJ dynamics has much in common with the motion of a particle in potential of the washboard type [4]

$$U(\phi) = -E_j(\cos\phi + i\phi - 1), \tag{26}$$

where i is the dc current expressed in the I_c (critical current) units, ϕ is the Josephson phase, and $E_j = \hbar I_c/2e$ is the Josephson energy. If the capacitance of the junction is sufficiently large, the junction may exhibit slowly decaying oscillations of the plasma phase at the bottom of the potential well (26). The frequency of these oscillations (plasma frequency) depends on the dc current and is given by formula (see, e.g., [4]),

$$\Omega_p = \left(\frac{2eI_c}{\hbar C}\right)^{1/2}(1-i^2)^{1/4}. \tag{27}$$

Relation (27) is usually satisfied for the JJ connected to a dc voltage source. If $I = I_c\sin\phi$, the theory exhibits perfect agreement with experiment [36]. However, there are deviations from the behavior predicted by Eq. (27) in the JJ characterized by anharmonic CPR. The anharmonicity may be caused by the simultaneous passage of both dc and ac currents of large amplitudes via the junction. Recently, Gronbech-Jensen *et al*. [37] studied the statistics of S → R switching of low-temperature tunnel JJ of the Nb–NbAlO$_x$–Nb type. The critical current in this system was determined for 10000 events.

The obtained results confirms the validity of relation (27) for the plasma frequency for small amplitudes of the ac current component. However, as the ac current amplitude grows, the agreement of formula (27) with the experimental values measured deteriorates, which can be related to the anharmonic character of the potential $U(\phi) = -E_j(\cos\phi - \alpha\cos 2\phi + i\phi - 1)$ at large ac current amplitudes. The theoretical investigation of the alternating current effect on the plasma frequency of the tunnel JJ simultaneously carrying dc and ac currents is presented below. The dynamics of a JJ can be described using the following equation (in this equation we use time units $\tau = \Omega_p(0)t$):

$$\ddot{\phi} + \frac{1}{\sqrt{\beta}}\dot{\phi} + \sin\phi + \alpha\sin 2\phi = i_d\sin\omega_d t\,. \tag{28}$$

For the calculation we will use $\phi = \phi_0 + \phi_1$, where ϕ_1 obeys equation

$$\dot{\phi} + \alpha\phi_1 = i + i_d\sin\omega_d t\,. \tag{29}$$

Using mathematical expressions described in [62]

$$\cos(a\sin\Omega t) = \sum A_n\exp(in\Omega t);\;\; A_n = J_{2k}(a)\,, \tag{30}$$

$$\sin(a\sin\Omega t) = \sum B_n\exp(in\Omega t);\;\; B_n = J_{2k+1}(a) \tag{31}$$

we obtain the following expression for plasma frequency of JJ with anharmonic CPR

$$\frac{\Omega_{pl}^2(a)}{\Omega_{pl}^2(0)} = \cos\phi_0 + 2\alpha J_0(a)\cos 2\phi_0\,. \tag{32}$$

In the last expression $J_0(a)$ is the Bessel function of zero order, $\Omega_p(0) = \sqrt{2eI_c/\hbar C}$, $a = i_d/(\alpha^2 + \omega_d^2)$. Equilibrium value ϕ_0 is determined from relation

$$\frac{i_0}{J_0(a)} = \sin\phi_0 + \alpha\sin 2\phi_0\,. \tag{33}$$

According to Eq. (32), an increase in the ac current component i_d results in decrease in the plasma frequency Ω_p. Thus, the presence of the ac component leads to renormalization of the plasma frequency (27) of the tunnel JJ.

The results of calculations according to Eqs. (32) and (33) are presented in the Fig. 17 by the solid and dashed curves, respectively, and compared with the experimental data (black circles) taken from [37]. Result of calculations of $\Omega_{pl}^2(\alpha)/\Omega_{pl}^2(0)$ as function of anharmonicity parameter α is presented in Fig. 17. Nonsymmetric character of $\Omega_{pl}^2(\alpha)$ is clear from calculations for different values of *a*. There is a minimum of $\Omega_{pl}^2(\alpha)/\Omega_{pl}^2(0) = 0.794$ at negative $\alpha = 0.3$ [63]. At positive values of anharmonicity parameter α plasma frequency $\Omega_{pl}^2(\alpha)$ decreases with increasing amplitude of oscillating part i_d. At negative values of anharmonicity parameter α influence of *a* on the plasma frequency $\Omega_{pl}^2(\alpha)$ is very small.

Results of calculations of $\Omega_{pl}^2(a)$ at different anharmonicity parameter α are presented in Fig. 18. At small α, the change in plasma frequency $\Omega_{pl}^2(a)$ is negli-

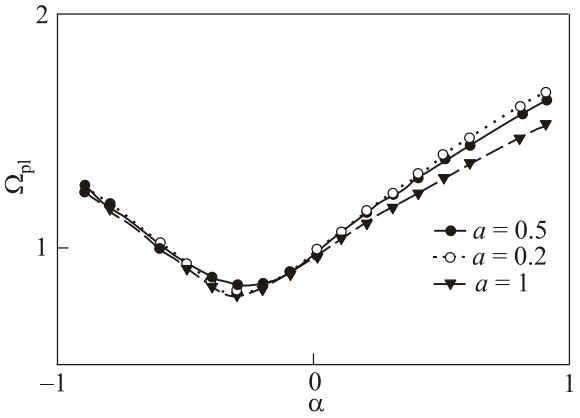

Fig. 17. Plasma frequency of JJ as function of anharmonicity parameter.

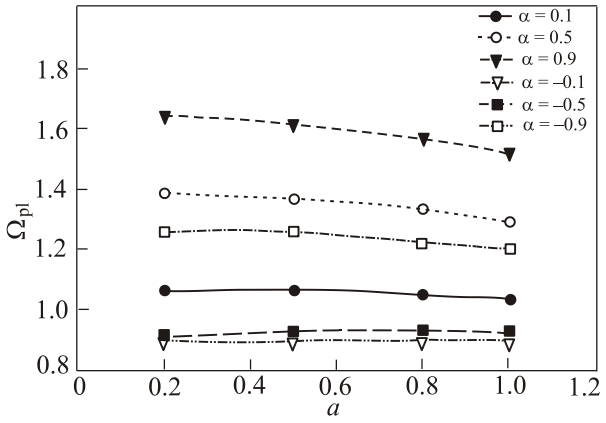

Fig. 18. Plasma frequency of JJ as function of amplitude of external ac current for different anharmonicity parameter.

gible, while at high α the influence of anharmonicity is important. At negative α influence of anharmonicity of CPR on plasma frequency is decreased.

3.3. Shapiro steps in I–V curve of JJ with anharmonic CPR

When radio-frequency signal is applied to Josephson junction, its *I–V* curve shows a set of Shapiro steps resulting from phaselocking of Josephson oscillations [64]. Analytical description of the Shapiro step dependence on the signal amplitude was obtained only for a high-frequency limit in the frame of RSJ model describing an overdamped junction with McCumber parameter $\beta_C << 1$ [4]. In particular, a nonsinusoidal CPR results in the generation of subharmonic Shapiro steps [65], which may lead to instabilities in modes of operation of Josephson voltage standards. Results of analytical and computational investigations of high-frequency dynamics of JJ characterized by nonzero capacitance ($\beta_C > 1$) and the second harmonic in the CPR are presented in [66]. Above presented Eq. (28) gives the result for step amplitude in harmonic case ($\alpha = 0$)

$$\Delta i_n = 2\left|J_n\left(\frac{a}{\omega\sqrt{(\omega\beta_C)^2+1}}\right)\right|, \tag{34}$$

where $J_n(x)$ is the Bessel function, a and ω are the amplitude and frequency of applied rf signal. The case of $\beta_C = 0$ coincides with the well known RSJ model [4]. In contrast to harmonic case ($\beta_C = 0$), there are subharmonic steps in *I–V* curve with amplitude (according to [66])

$$\Delta i_{(2n+1)/2} = 2\beta\left|\frac{J_n\left(\frac{a}{\omega\sqrt{(\omega\beta_C)^2+1}}\right)J_{n+1}\left(\frac{a}{\omega\sqrt{(\omega\beta_C)^2+1}}\right)}{\sqrt{(\omega\beta_C)^2/4+1}}\right|. \tag{35}$$

For JJ with anharmonic CPR ($\alpha \neq 0$) the following expression for harmonic Shapiro step amplitudes is obtained as [66]:

$$\Delta i_n = 2\max\left|J_n\left(\frac{a}{\omega\sqrt{(\omega\beta_C)^2+1}}\right)\sin\phi + \alpha J_{2n}\left(\frac{a}{\omega\sqrt{(\omega\beta_C)^2+1}}\right)\sin 2\phi\right|, \tag{36}$$

and for subharmonic steps as

$$\Delta i_{1/2} = 2\max\left|\sin\phi\left[\alpha J_1\left(\frac{2a}{\omega\sqrt{(\omega\beta_C)^2+1}}\right)+\beta_C\frac{J_1\left(\frac{a}{\omega\sqrt{(\omega\beta_C)^2+1}}\right)J_0\left(\frac{2a}{\omega\sqrt{(\omega\beta_C)^2+1}}\right)}{\sqrt{(\omega\beta_C)^2/4+1}}+\right.\right.$$
$$\left.\left.+\,4\alpha^2\beta_C\frac{J_0\left(\frac{2a}{\omega\sqrt{(\omega\beta_C)^2+1}}\right)J_2\left(\frac{2a}{\omega\sqrt{(\omega\beta_C)^2+1}}\right)}{(\omega\beta_C)^2+1}\cos\phi\right]\right|. \tag{37}$$

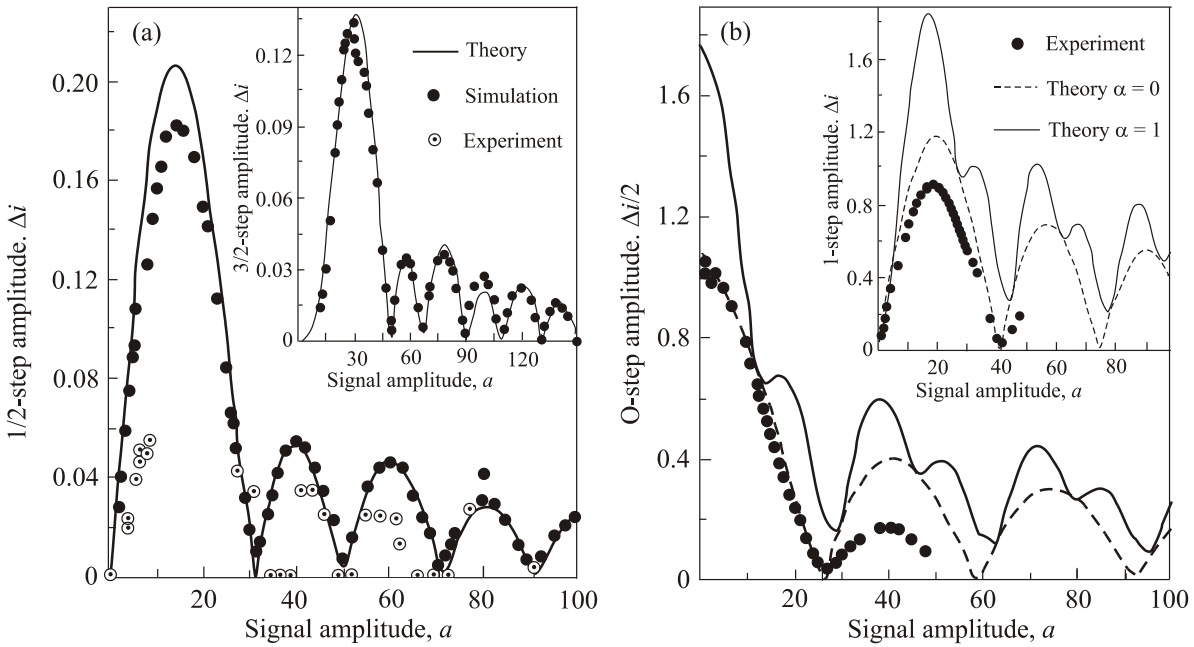

Fig. 19. Dependencies of the 1/2- and 3/2-step amplitudes on the applied signal amplitude a at frequencies $\omega = 0.611$, $\beta = 35$ and $\alpha = 0$. Solid line corresponds to Eq. (35), filled dots correspond to numerical simulation, and empty dots correspond to experimental results for the c-oriented Nb/Au/YBCO junctions (a). Dependencies of the critical current amplitude $\Delta i/2$ (0-step) and the 1-step amplitude Δi (in inset) on the applied signal amplitude a at frequency $\omega = 1.62$ and $\beta = 4$. Dashed and solid lines correspond to formula (36) at $\alpha = 0$ and $\alpha = 1$, the filled dots correspond to experimental results for the c-tilted Nb/Au/YBCO junctions (b).

Figures 19 and 20 present the analytical results, as well as experimental data for both c-oriented and c-tilted Nb/Au/YBCO junctions formed on NdGaO substrates (junction areas ranged from 10·10 μm^2 to 30·30 μm^2) [67,68]. Similar results for subharmonic Shapiro steps were obtained in [69] for c axis $YBa_2Cu_3O_{7-x}$/Pb tunnel junctions.

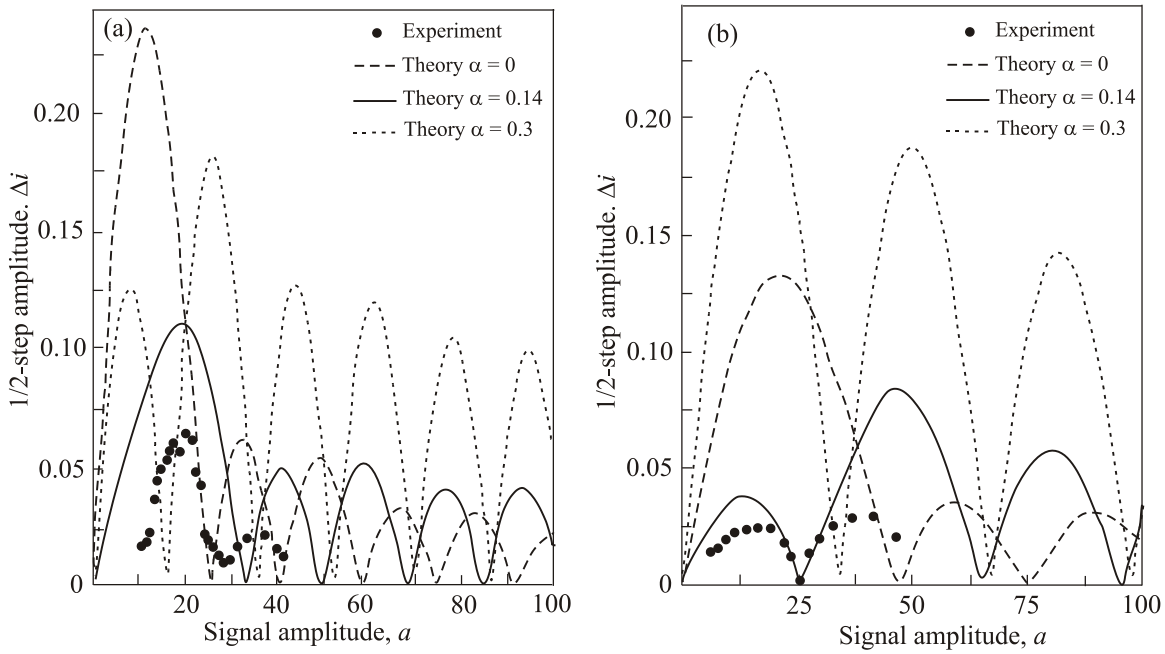

Fig. 20. Dependence of the 1/2-step amplitude Δi on the applied signal of amplitude a at $\beta = 4$ for frequencies $\omega = 1.62$ (a) and $\omega = 2.2$ (b). Dashed, solid and dotted lines correspond to the step behavior according to formula (37) with $\alpha = 0$, $\alpha = 0.14$, and $\alpha = 0.3$, respectively. The filled dots are experimental data for the c-tilted Nb/Au/YBCO junction.

3.4. Inluence of anharmonic CPR on long JJ dynamics

Physical properties of magnetic flux dynamics in long JJ play an important role in the modern superconductivity related electronics. We consider a long JJ, where the word "long" means that we take into account the variation of the phase along one of the spatial coordinates, i.e., along x. Further, it will become clear that opposite to the case of the usual JJ with only first harmonic in CPR, there is no universal length scale at which the phase changes or at which the weak magnetic field is screened. Moreover, depending on the state, the characteristic scale of x variation affecting magnetic field screening can be different, so the junction can be small if it is in one state and it can be long in another state. At the same time, in order to neglect the spatial variation of the phase along the junction width (y direction), we assume that the junction is short in the y direction in all states. The calculation of static magnetic flux distributions in the long JJ with consideration of the anharmonic CPR was carried out in [58,70–72]. This model is described by the double sine-Gordon equation (2SG) for magnetic flux distribution in the static regime

$$-\phi'' + \sin\phi + \alpha\sin 2\phi = \gamma; \qquad x \in (-l, l) \tag{38}$$

with the boundary conditions in the following form

$$\phi'(\pm l) = h_e\,. \tag{39}$$

The magnitude ϕ is the external current, l is the semilength of the junction. I_c and α are parameters corresponding to contributions of 1st and 2nd harmonic, respectively. h_e is external magnetic field. Stability analysis of $\psi(x, p)$ is based on numerical solution of the corresponding Sturm–Liouville problem

$$-\psi'' + q(x)\psi = \lambda\psi; \qquad \phi'(\pm l) = 0\,, \tag{40}$$

with potential $q(x) = \cos x + 2\alpha\cos 2x$. The minimal the eigenvalue $\lambda_0(p) > 0$ corresponds to the stable solution. In case when $\lambda_0(p) < 0$ the solution $\phi(x, p)$ is unstable. The case when $\lambda_0(p) = 0$ indicates the bifurcation with respect to one of parameters $p = (l, \alpha, h_e, \gamma)$. Results of investigations carried out in [70–72] shows that consideration of the second harmonic significantly changes the shape and stability properties of trivial and fluxon static distribution in long JJ.

In the "traditional" case $\alpha = 0$ two trivial solutions $\phi = 0$ and $\phi = \pi$ (denoted by M_0 and M_π, respectively) are known at $\gamma = 0$ and $h_e = 0$. Consideration of the second harmonic $\alpha\sin 2\phi$ leads to appearance of two additional solutions $\phi = \pm\arccos(-1/2\alpha)$ (denoted as $M_{\pm ac}$). The corresponding λ_0 as functions of 2SG-equation coefficients have the form $\lambda_0[M_0] = 1 + 2\alpha$, $\lambda_0[M_\pi] = -1 + 2\alpha$, and $\lambda_0[M \pm ac] = \alpha[1 - (1/2\alpha)^2]$. The exponential stability of these constant solutions is determined by the signs of the parameters and by the α [70–72] (Fig. 21). The full energy associated with the distribution of $\phi(x)$ is calculated using the expression:

$$F(p) = \int_{-l}^{l}\left[\frac{\phi'^2}{2} + 1 - q(x) - \gamma\phi\right]dx - h_e\Delta\phi\,, \tag{41}$$

Fluxon solution of Eq. (38) in the case of $h_e = 0$ and $\gamma = 0$ at $l \to \infty$ has a form [73]:

$$\Phi^{\pm}_{\infty} = \phi(x) = 4\arctan(\exp(\pm x)) + 2\pi n \tag{42}$$

where "+" sign corresponds to fluxon, "–" sign corresponds to antifluxon. At small external fields h_e such distributions are fluxon Φ^1, antifluxon Φ^{-1} and their bound states $\Phi^1\Phi^{-1}$ and $\Phi^{-1}\Phi^1$. As external magnetic field h_e grows, more complicated stable fluxon and bound states appear: $\Phi^{\pm n}$ and $\Phi^{\pm nn}$ $(n = 1, 2, 3, ...)$.

The energy of one-fluxon distribution Φ^1 converges to unity $F(\alpha \to 0) \to 1$ which corresponds to an energy of a single fluxon Φ^1_∞ in a traditional "infinite" junction model at $\alpha = 1$. With change of α the number of fluxons

$$N(p) = \frac{1}{2\pi l}\int_{-l}^{l}\phi(x)dx \tag{43}$$

corresponding to the distribution Φ^1 is conserved, i.e., $\partial N/\partial\alpha = 0$. Here we have $N[\Phi^1] = 1$. Results of influence of second harmonic CPR in $\lambda_0(h_e)$ were calculated in [70–72] and presented in Figs. 22, 23. Simulation results show that consideration of the second harmonic in CPR

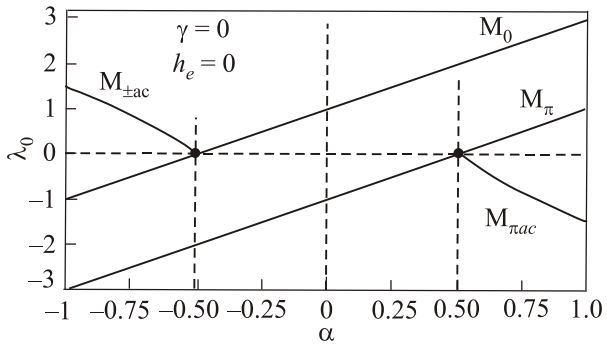

Fig. 21. Stability region as a function of anharmonicity parameter.

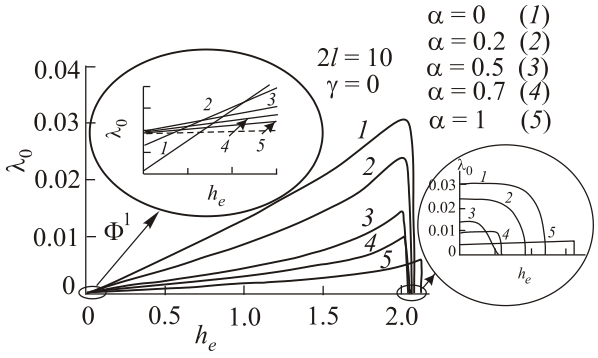

Fig. 22. Dependence of $\lambda_0(h_e)$ for Φ^1 with increasing of anharmonicity parameter α. $2l = 10$, $\gamma = 0$.

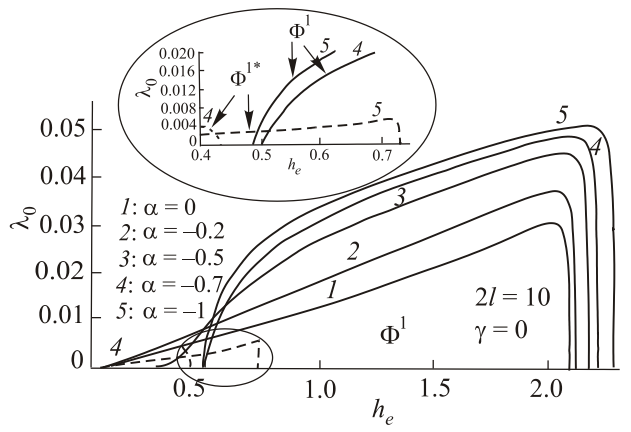

Fig. 23. Dependence of $\lambda_0(h_e)$ for one fluxon states Φ^1 and Φ^{1*} with increasing of anharmonicity parameter α. $2l = 10$, $\gamma = 0$.

significantly changes the shape and stability properties of fluxon static distribution in long JJ.

4. Qubits based on JJ with anharmonic CPR

4.1. Qubits

The great majority of Josephson and SQUID research since the beginning of the XXI century has focused on possible applications in the field of quantum computation [74,75]. In classical digital computation, the processor takes as its input ones and zeros (coded, in the case of silicon integrated circuits, as two distinct voltage levels) and derives an output by performing some kind of classical Boolean logical operation on this input. In contrast to it, in quantum computation the processor takes as its input a quantum coherent superposition of ones and zeros [74,75]. The quantum processor then performs a quantum mechanical operation on this input state in order to derive an output which is also a quantum coherent superposition. The basic element of a quantum computer is known as a qubit. The state of the qubit, $|\psi\rangle$ is a linear superposition of the two quantum basis states $|0\rangle$ and $|1\rangle$ [74,75]. Realization of qubits based on JJ and their application requires the millikelvin temperature region. As follows from above presented discussion, the anharmonic character of CPR becomes important at this temperature and therefore anharmonicity must be taken into account in discussion of JJ qubits. This conclusion is also supported by investigations [44,76].

In order to analyze the qubits with JJ, one has to solve the corresponding stationary Schrödinger equation with an appropriate boundary condition

$$H\Psi = E\Psi\,, \qquad (44)$$

where H is the Hamiltonian operator, Ψ is the wavefunction, and E is the eigenenergy. Quantum dynamics of an isolated JJ is described with the Mathieu–Bloch picture for a particle moving in a periodic potential, similar to the electronic solid state theory [4]. In this section, we shall describe the quantum dynamics of two types of qubits: phase and charge qubits. Such qubits have distinct limiting regimes: the phase regime $E_j \gg E_c$, is analogous to the tight-binding approximation, and the charge regime, $E_j \ll E_c$, is analogous to the near-free particle approximation. At the end of this section, we also shall discuss a flux qubits using low inductance interferometer with anharmonic JJ [77,78,80,90].

As mentioned in previous studies (i.e., [4, 81,82]), the wavefunction should satisfy the periodic boundary condition $\Psi(\phi) = \Psi(\phi + 2\pi)$. Therefore, the required boundary condition for solving Eq. (44) can be expressed as

$$\Psi(a) = \Psi(b), \quad \Psi'(a) = \Psi'(b)\,,$$

where $a = \theta_{\min}$ and $b = \theta_{\min} + 2\pi$ are the lower and upper bounds such that a and b depend on the variation of i_b as well as α. Note that the value of a and b are different for phase and charge qubits. Additional details about a and b are given below.

4.1.1. Phase qubit with anharmonic CPR. A circuit model of a phase qubit system using single JJ is shown in Fig. 24. Corresponding Hamiltonian of the system [81,83] associated with anharmonic CPR can be written as [82]

$$H = -E_c \frac{\partial^2}{\partial\phi^2} + E_j[i_b\phi + \cos\phi - \frac{\alpha}{2}\cos 2\phi]\,, \qquad (45)$$

where $i_b = I_b/I_c$ is the ratio of the bias currents applied to the system, ϕ denotes the phase difference, E_c is the electrostatic energy, and E_j is the Josephson coupling energy. In some models suggested in [78] and [80], CPR of Josephson junctions includes second and third harmonics.

The presence of second harmonic in CPR leads to hump like shape of potential energy which seems to be very important for the manipulation with phase qubit. Figure 25 illustrates the influence of second harmonic on the potential

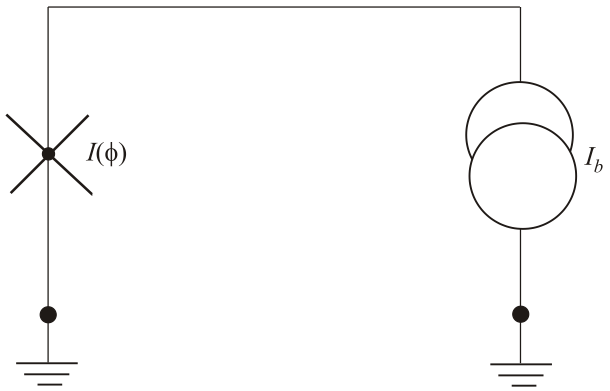

Fig. 24. Circuit model of a phase qubit. The crossed lines indicate the junction. I_b is the bias current source.

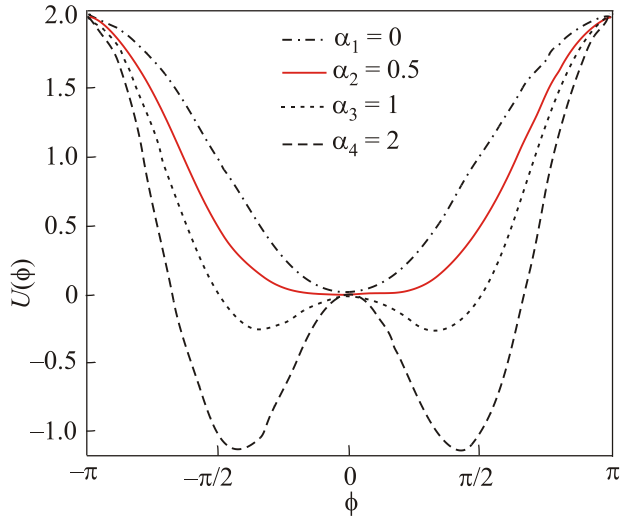

Fig. 25. Potential energy $U(\phi)$ of anharmonic JJ.

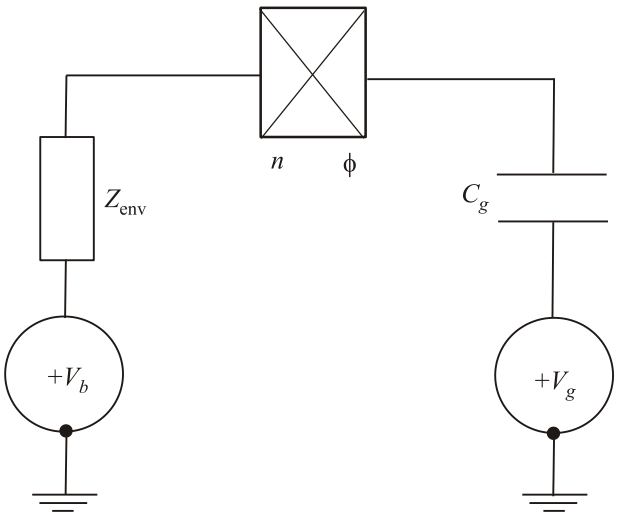

Fig. 26. Circuit model of a charge qubit. The crossed box indicates the combination of the tunnel element and the junction capacitor C_j connected parallel. The gate charge is $Q_g = 2en_g = C_gV_g$.

$$U(\phi) = 1 - \frac{\alpha}{2} - \cos(\phi) + \frac{\alpha}{2}\cos(2\phi)\,, \qquad (46)$$

for various values of α. For instance, the potential has a single minimum at $\phi = 0$ for $\alpha \le 0.5$. and double minima for $\alpha > 0.5$ in the ranges $-\pi < \phi < 0$ and $0 < \phi < \pi$, respectively. The authors in [58] and [84] also discussed how $U(\phi)$ changes from single potential well to double potential well in the case of π junctions (i.e., the junctions with negative critical current).

After substituting Eq.(45) into the Schrödinger Equation (44), we can obtain Mathieu eigenvalue equation for zero bias current case:

$$\frac{d^2\Psi}{d\phi^2} + \frac{E_j}{E_c}\left\{\cos\phi - \frac{\alpha}{2}\cos 2\phi\right\}\Psi = -\varepsilon\Psi, \qquad (47)$$

where $\varepsilon = E/E_c$. Equation (47) is called the Mathieu eigenvalue equation, it describes the properties of phase qubit under the periodic boundary condition with lower bound $a = 0$ and upper bound $b = 2\pi$.

4.1.2. Charge qubit with anharmonic CPR. A circuit model of a charge qubit system using single JJ is shown in Fig. 26. The Hamiltonian of the charge qubit system [81,83] with anharmonic CPR can be written as

$$H = E_c(\hat{n} - n_g)^2 - E_j\left\{i_b\phi + \cos\phi - \frac{\alpha}{2}\cos 2\phi\right\}, \qquad (48)$$

where $E_c = Q_g^2/(2C_\Sigma)$ is the electrostatic energy (Cooper pair charge energy) that depends on gate voltage V_g and the capacitor $C_\Sigma = C_g + C_j$, and $E_j = \hbar I_c/(2e)$ is the Josephson coupling energy in terms of critical current of Josephson junction I_c. Introduced $\hat{n} = -i(\partial/\partial\phi)$ is the dimensionless momentum operator that refers to the number of Cooper-pair on the island and has a physical meaning of charge Q accumulated on the junction capacitor C_j in the units of double electronic charges (i.e., $\hat{Q} = 2e\hat{n}$). Furthermore, $n_g = C_gV_g/(2e)$ is the dimensionless charge number used to externally control the system [85]. Figure 26 illustrates a single Cooper pair box for a charge qubit including a gate voltage V_g and a gate capacitance C_g.

Using washboard potential from Eq. (46) for nonzero bias current as well as α, we can determine the upper and lower bounds of the periodicity interval finding roots of equation

$$f(\phi) = \frac{dU}{d\varphi} = -i_b + \sin\phi - \alpha\sin 2\phi = 0$$

that sets condition for $U(\phi)$ stable minimum $\phi_{\min}$. In this case, the interval for periodic boundary will be $a = \phi_{\min}$ and $b = \phi_{\min} + 2\pi$. Periodical solutions in the case of nonzero bias current were discussed in detail in [4] and [82] using wavepacket approach.

After substituting Eq. (48) into the Schrödinger equation as in Eq. (44), we can obtain a Mathieu-type eigenvalue equation:

$$\frac{d^2\Psi}{d\phi^2} - p\frac{d\Psi}{d\phi} + q\Psi = -\varepsilon\Psi, \qquad (49)$$

where $\varepsilon = E/E_c$, the terms $p = 2in_g$ and

$$q(\phi) = \frac{E_j}{E_c}\left[i_b\phi + \cos\phi - \frac{\alpha}{2}\cos 2\phi\right] - \frac{|p|^2}{4}.$$

Here, we will present the evaluation of expectation values of the supercurrent operator given in equation $\hat{I}_s/I_c = \sin\phi - \alpha\sin 2\phi$ and the number operator $\hat{n} = -i(\partial/\partial\phi)$ within the interval $[a,b]$ in the lowest band for the charge qubit.

First of all, the expectation value of supercurrent [86] can be obtained from

$$i_s = \langle \Psi | \hat{I}_s / I_c | \Psi \rangle = \frac{1}{b-a} \int_a^b \Psi^* \{ \sin\phi - \alpha \sin 2\phi \} \Psi d\phi. \quad (50)$$

Similarly, the expectation value of number operator $\hat{n}$ can be determined as

$$\langle \hat{n} \rangle = \langle \Psi | \hat{n} | \Psi \rangle = \frac{1}{b-a} \int_a^b \Im \left\{ \Psi^* \frac{\partial \Psi}{\partial \phi} \right\} d\phi. \quad (51)$$

The Mathieu-type eigenvalue problems defined in Eqs. (47), (49) can be discretized using the finite difference approach discussed in [81] on a discrete lattice:

$$e\Psi_{j-1} + f_j \Psi_j + e^* \Psi_{j+1} = \lambda \Psi_j, \ \forall j = 0,1,2,...,N-1.$$

The problem is that we want to get rid of the upper and lower end wavefunctions ($\Psi_{-1} = \Psi_{N-1}$ and $\Psi_N = \Psi_0$) in the form of boundary conditions given in Eq. (44). After that, through mathematical discretization of these equations we can approximate the continuum behavior of the system to obtain the eigenvalue problem of the form:

$$\mathbf{A}_0 \Psi_n = \lambda_n \Psi_n, \quad n = 0,1,2,\ldots, \quad (52)$$

where Ψ_n is an eigenfunction associated with eigenvalue λ_n for an arbitrary eigenstate n; and $\mathbf{A}_0$ is a complex $N \times N$ periodic tridiagonal coefficient matrix,

$$\mathbf{A}_0 = \begin{pmatrix} f_0 & e^* & 0 & 0 & 0 & \cdots & 0 & e \\ e & f_1 & e^* & 0 & 0 & \cdots & 0 & 0 \\ 0 & e & f_2 & e^* & 0 & \cdots & 0 & 0 \\ 0 & 0 & e & f_3 & e^* & \cdots & 0 & 0 \\ 0 & 0 & 0 & e & f_4 & \cdots & 0 & 0 \\ \vdots & \vdots & \vdots & \vdots & \vdots & \vdots & \vdots & \vdots \\ 0 & 0 & 0 & 0 & 0 & \cdots & f_{N-2} & e^* \\ e^* & 0 & 0 & 0 & 0 & \cdots & e & f_{N-1} \end{pmatrix} \quad (53)$$

The coefficients of the periodic tridiagonal matrix in Eq. (53) are:

$$e = 1 + hp/2, \quad f_j = (h^2 q_j - 2), \quad \lambda = -h^2 \varepsilon, \quad h = \frac{b-a}{N+1}, \quad (54)$$

where e^* is the complex conjugate and h is the step size in the discretization scheme.

Throughout this study, the numerical solution of Eq. (52) is calculated using the conventional LAPACK eigenvalue solver. Note that the coefficient matrix in Eq. (53) requires an $N + 2$ data storage space in its present form. In the literature ([87] and [88]) the linear system solution with a real symmetric periodic tridiagonal coefficient matrix is widely studied, but the eigenvalue problem [81] formulated in the present study requires an efficient design and stable algorithm for finding the eigenvalues of such a matrix. The number of subintervals is preferred to be $N = 3000$ with sufficient accuracy, the reason and preference of it will be explained.

4.2. Influence of anharmonic CPR on qubit characteristics

4.2.1. Phase qubit. The analysis in [78] was limited to asymptotical solutions of Mathieu equations. Here, we performed a full numerical analysis of Mathieu equation (47) with inclusion of second harmonic in phase qubit regime (i.e., $E_j/E_c \gg 1$). As follows from the results, all energy levels split into two sub-levels $\varepsilon_i^{\pm} = \varepsilon_i \pm \Delta_i$. Energy spectrum of Mathieu equations for $i = 0, 1$ evaluated using numerical calculations presented in Fig. 27 coincides with the results in [78]. The ground ($i = 0$) and first ($i = 1$) states of the energy spectrum were obtained and it is shown that splitting in the ground and first excited state depends on the anharmonicity parameter α. For high values of energy scale $E_j/2E_c$, the splitting between $\alpha = 0$ and $\alpha \neq 0$ cases becomes large. On the other hand, it can be seen from the calculations that the change in splitting of ground state is

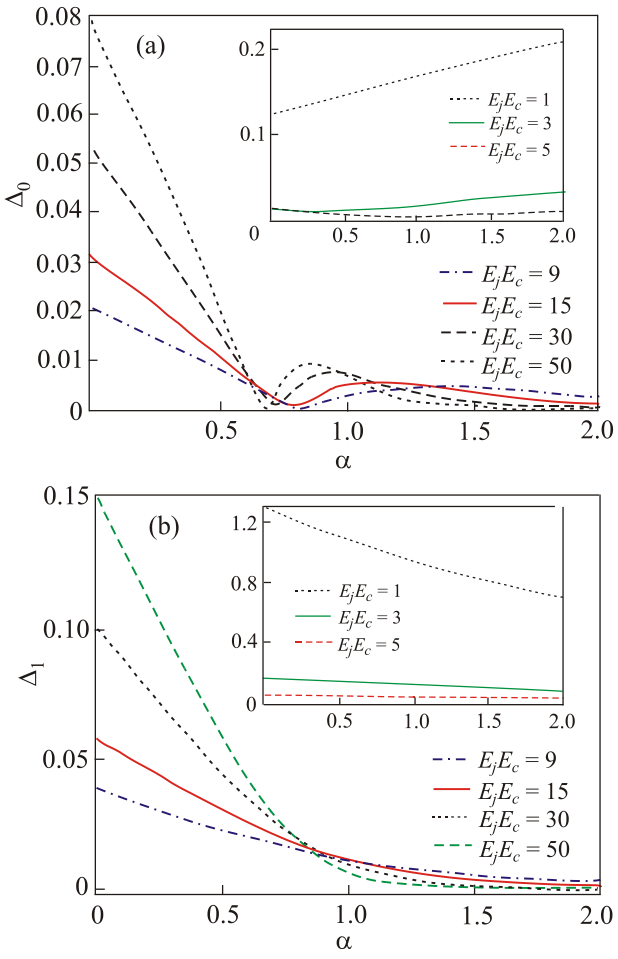

Fig. 27. (Color online) Splitting parameters versus anharmonicity α of the CPR. Splitting of the ground state (a), first excited state (b).

smaller than the change of the first level. This means that the first state is more sensitive to anharmonicity parameter α.

Furthermore, the numerical modeling is carried out to analyze the influence of the control parameters on the splitting of energy states $\Delta_i = \varepsilon_i^+ - \varepsilon_i^-$. Figure 27 presents the behavior of the splitting of energy states Δ_i for various energy scales E_j/E_c. The results for Δ_0 are presented in Fig. 27(a) within the range $0 \le \alpha \le 2$. As was mentioned before, the authors in [78,89] found similar results for dc-SQUID from an oscillatory model analytically. Unlike our results, their findings are limited to the range $0.5 \le \alpha \le 1.5$ for Δ_0. In contrast to [78,89], we observed fine structure in dependence of $\Delta_0(\alpha)$ for different E_j/E_c values. For small anharmonicity parameter (i.e., $\alpha < 0.65$), the splitting parameter Δ_i decreases linearly with increasing α. The results for Δ_i are in good agreement with findings of solid state theory. Fixing the amplitude of first harmonic by negative sign of second harmonic leads to an approximate linear decreasing of $\Delta_0(\alpha) \approx E_j(1-\alpha)$ [90]. Similar behavior of linear decreasing in Δ_0 is obtained in our numerical results presented in Fig. 27(a). However, compared to approximate result, the vanishing point of Δ_0 is located in the range $0.6 < \alpha < 0.9$ for various energy scales. This is because numerical results are more precise than the results obtained from preceding approximate expression. In addition, $U(\phi, \alpha)$ in Fig. 25 has a single minimum for $\alpha \le 0.5$ while it has two minima for $\alpha > 0.5$.

As discussed before for Fig. 25, the shape of the potential was switched from a single well to a double well structure for $\alpha > 0.5$. For higher values of energy scale such as $E_j/E_c \ge 9$, the behavior of $\Delta_0(\alpha)$ illustrates different tendencies. For instance, $\Delta_0(\alpha)$ keeps decreasing from $\alpha = 0.5$ to $\alpha = \alpha_{cr}$ until it vanishes. The values of α_{cr} are determined from our calculation (see Fig. 27(a)) as 0.6231, 0.6007, 0.5784, and 0.5634 for energy scales 9, 15, 30, and 50, respectively. The "hump" of the double well potential is not so high in this region and the energy levels are strongly coupled. Such behavior corresponds to two-level crossing. On the other hand, for $\alpha_{cr} < \alpha \le \alpha_{max}$ where α_{max} is given in Table 2, $\Delta_0(\alpha)$ has an increasing tendency as shown in Fig. 27(a). For $\alpha > \alpha_{max}$ the "hump" of the double well increases so the energy levels become weakly coupled. Consequently, the second harmonic in Eq. (46) becomes dominant and leads to a two-level crossing.

For large values of anharmonicity parameter ($0.65 < \alpha$), we obtain results similar to those in [78]. The maximum values of $\Delta_0(\alpha)$ peaks at different energy scales are given in Table 2.

Table 2. Changing of the maximum of $\Delta_0(\alpha)$ peaks

E_J/E_C	α_{max}	$\Delta_{0\,max}$
9	1.350	0.0045
15	1.125	0.0054
30	0.950	0.0072
50	0.875	0.0090

As also shown in Fig. 27, the peak position of Δ_0 depends on the energy scale E_j/E_c. Besides, the width of the peak grows with decreasing energy scale E_j/E_c in phase qubit regime. With decreasing E_j/E_c, the peak value of $\Delta_0(\alpha)$ is also suppressed. As shown in the inset of Fig. 27(a), $\Delta_0(\alpha)$ only reveals tendency for growth when $E_j/E_c < 3$ for charge qubit regime. Figure 27(b) illustrates similar results for Δ_1. As can be seen from this figure, $\Delta_1(\alpha)$ reveals monotonic decreasing behavior with an increase in the anharmonicity parameter α for all E_j/E_c.

The influence of the energy scale E_j/E_c on splitting of energy state Δ_i for fixed value of anharmonicity parameter α is presented in Fig. 28. This plot clearly illustrates an upward trend of Δ_i for $E_j/E_c > 50$. The reason for restricting E_j/E_c up to 50 is related to technological achievement in the realization of JJ with a very small capacitances (at a level of femto Farad (fF)) [85]. The energy splitting in ground state Δ_0 increases for energy scale $E_j/E_c > 3$. The partial derivative of Δ_0 with respect to energy scale for various α is plotted in Fig. 29. As follows from Fig. 28 and Fig. 29, high slope corresponds to the

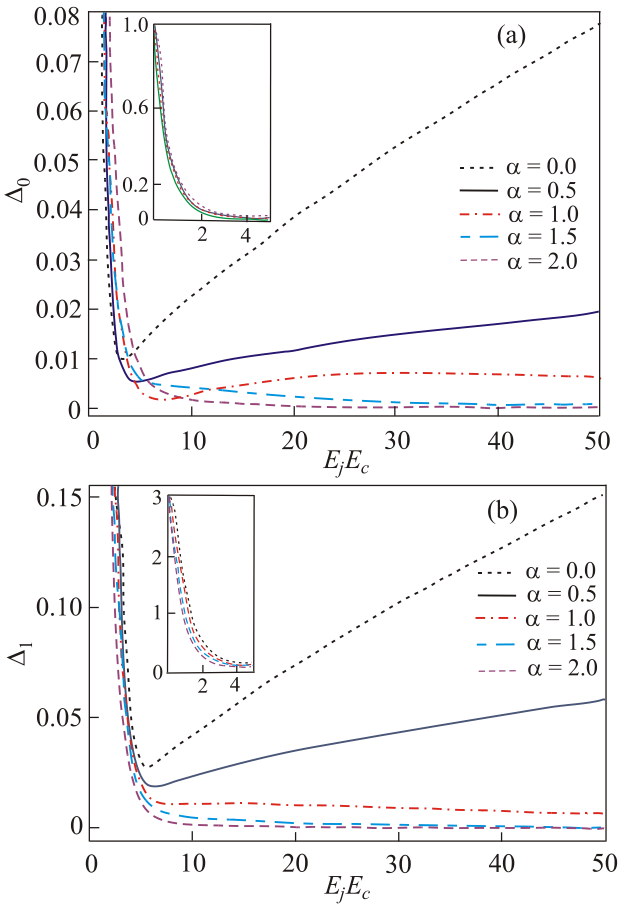

Fig. 28. (Color online) Splitting versus energy scale. Splitting of the ground state (inset shows behavior of Δ_0 for the range $0 \le E_j/E_c \le 4$) (a). Splitting of the first excited state (inset shows behavior of Δ_1 for the range $0 \le E_j/E_c \le 4$) (b).

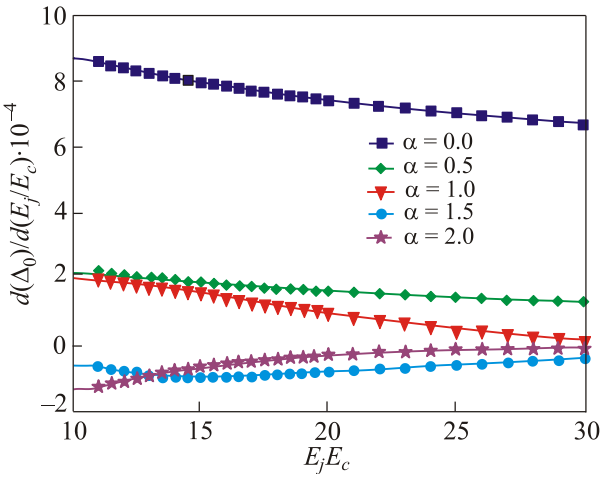

Fig. 29. (Color online) Differential plot for the splitting parameters in the ground state.

case of harmonic CPR ($\alpha = 0$). Increasing α up to 2 results in fall of the slope down to zero.

As follows from the inset of Fig. 28(a), at small $E_j/E_c < 3$, Δ_0 sharply decreases with an increase in E_j/E_c. Another peculiarity of this region is related to non-sensitivity of results to changing of amplitude of second harmonic α. The influence of the energy scale parameter E_j/E_c on splitting of energy state Δ_1 for fixed α value is presented in Fig. 28(b). The splitting of first state $\Delta_1(E_j/E_c)$ reveals behavior similar to the case $\Delta_0(E_j/E_c)$. The inset in Fig. 28(b) shows that at small $E_j/E_c < 3$, Δ_1 decreases sharply with an increase in E_j/E_c similar to Δ_0. Notice that differential plots for the first level also resemble those shown in Fig. 29.

4.2.2. Charge qubits. As mentioned before, the energy scale $E_j/E_c < 1$ corresponds to the single Cooper box (SCB) charge qubit limit. In this limit, energy spectrum can be described at quasi-charge approach [4,81] similar to quasi-momentum representation in solid-state theory [90] (see also inset Fig. 20(a). Energy gap Δ_0 dependence on anharmonicity parameter α presented in Fig. 30(a) resembles the phase qubit case in Fig. 27. Similarly to Δ_0 which is the difference between ε_1 and ε_0 at $n_g = 0.5$, the "secondary energy gap" Δ_1 is the difference between ε_2 and ε_1 at $n_g = 1$. The detailed description can be found in [81]. Notice that Δ_i refers to energy gap in charge qubit whereas it refers to splitting of energy states in phase qubit. In Fig. 30(b), the dependence of gap parameters Δ_i on energy scale E_j/E_c is illustrated. This result qualitatively is also in good agreement with Fig. 28. However, in case of SCB the growth of Δ_i with E_j/E_c has revealed a nonlinear behavior.

The expectation value of number operator $\langle\hat{n}\rangle$ given in Eq. (51) is plotted with respect to gate number n_g in Fig. 31 at small bias current $i_b = 0.1$. The $\langle\hat{n}\rangle$ vs n_g is experimentally observed for SCB in [91] for junction parameters $E_c = 0.215$ meV and $E_j/E_c = 0.16$. As follows from Fig. 31 dependence of $\langle\hat{n}\rangle$ vs n_g is not sensitive

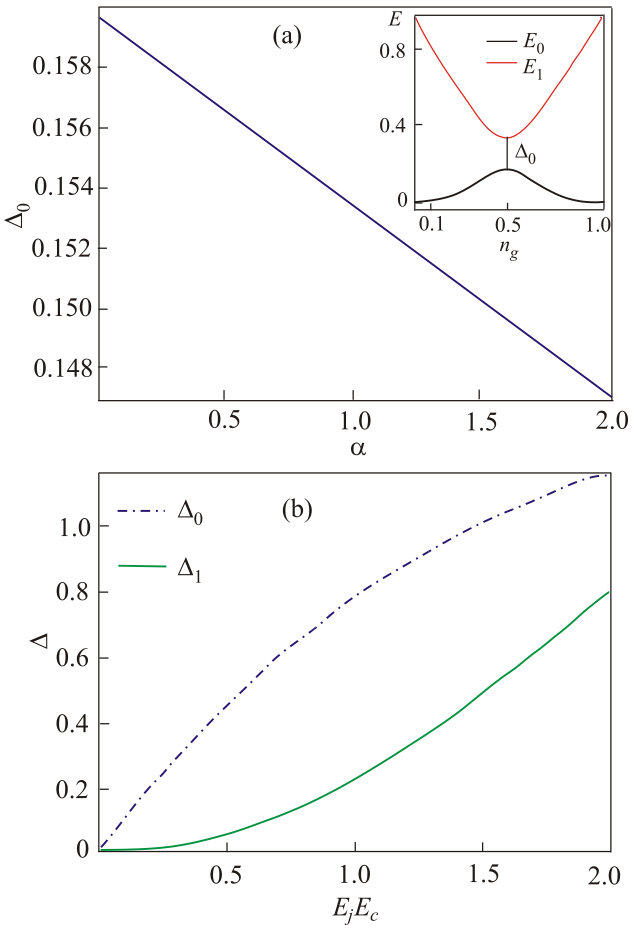

Fig. 30. (Color online) Results for the charge qubit obtained at $n_g = 0.5$.

to α. The expectation value of supercurrent $i_s = \langle\hat{I}/I_c\rangle$ versus n_g is illustrated in Fig. 32 for different anharmonicity parameters α. The positions of the peaks in i_s vs n_g relation is the same as the peaks for $\alpha = 0$ in [81]. Note that the supercurrent is equal to zero when the bias current i_b is set to zero. The peaks at half-integer n_g values correspond to the tunneling of Cooper pairs from one

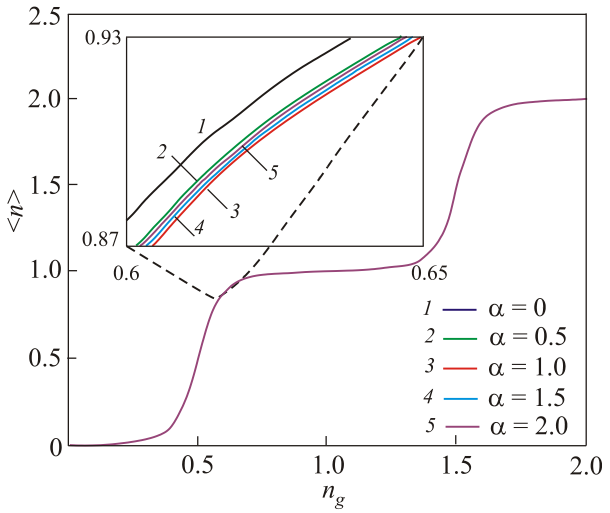

Fig. 31. (Color online) $\langle n\rangle$ versus n_g for $i_b = 0.1$.

electrode to another. When we compare Fig. 32(a) and 32(b), the increasing of i_b leads to an increase in the magnitude of i_s while the increasing of anharmonicity parameter α leads to a decrease in the magnitude of i_s.

It was shown in [54] that the anharmonicity of the CPR is equivalent to the introduction of an effective inductance connected in series to the JJ. The value of effective inductance is proportional to the magnitude of the anharmonicity parameter. This implies that such additional inductance leads to an increase in the impedance of the circuit for charge qubit. For that reason, the amplitude of the expectation value of supercurrent i_s in Fig. 32 is suppressed with increasing α.

4.2.3. Silent qubit. The silent qubit is just a low-inductive two-junction interferometer based on JJ with anharmonic CPR and does not require application of half-flux quantum. Such a qubit is called "silent" because of both its high protection against external magnetic field impact and the absence of any state-dependent spontaneous circular currents. The potential energy of such quantum-mechanical system was described in the papers [66,78,79,80]. As shown in this work and mentioned in section 2, presence of second harmonic in CPR of JJ leads to a two-hump potential

$$U(\phi,\phi_+) = -\frac{\Phi_0 I_{c1}}{2\pi}\left[\cos\left(\frac{\phi}{2}+\phi_+\right) - \frac{\alpha_1}{2}\cos(\phi+2\phi_+)\right] - \frac{\Phi_0 I_{c2}}{2\pi}\left[\cos\left(\frac{\phi}{2}-\phi_+\right) - \frac{\alpha_2}{2}\cos(\phi-2\phi_+)\right], \quad (55)$$

where $\phi = \phi_1 - \phi_2$ is difference of the JJ phases, $\phi_+ = (\phi_1+\phi_2)/2$, $\phi_e = 2\pi(\Phi/\Phi_0)$ are normalized external fluxes. In the absence of external magnetic field one can easily obtain the conditions leading to the double-well energy potential formation (see above). If both junctions (with the same CPR) are of the same size, the energy potential remains always symmetric and any state-dependent current is impossible even if an external magnetic field is applied. However, at different sizes of the junction (different critical currents) the external magnetic field always breaks the potential symmetry and produces a state-dependent current in the loop. In papers [66,77,79,80] influence of external magnetic field on the splitting of energy levels was investigated. It was shown that the ratio E_J/E_Q also has influence on splitting of energy levels. The value of external magnetic field Φ_e, in which splitting parameter remains unchangeable was found. In these papers examples of some logic operations using silent qubit are also considered.

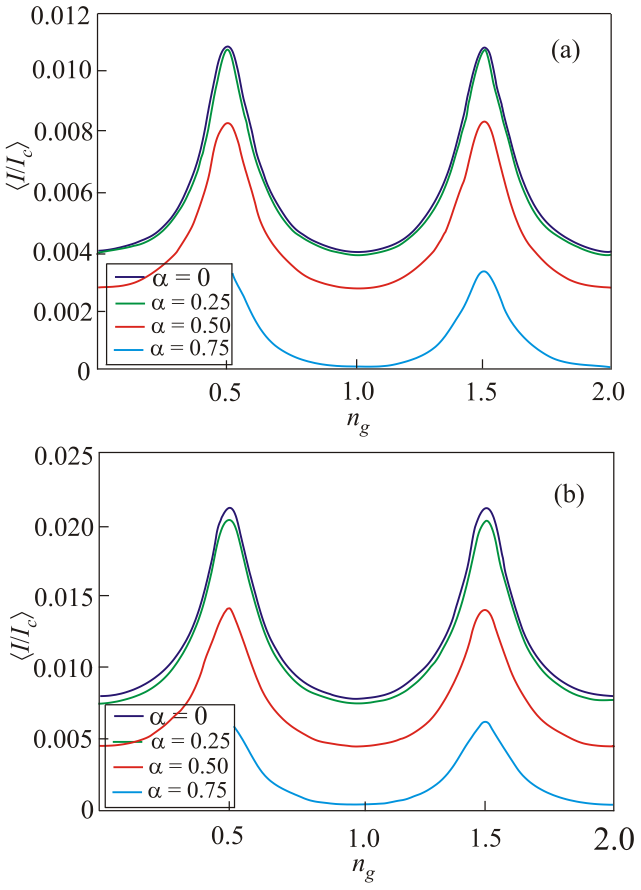

Fig. 32. (Color online) Expectation value of supercurrent $\langle I/I_c \rangle$. i_b =0.05 (a), i_b = 0.1 (b).

5. Conclusions

Results of theoretical and experimental investigations of different JJ with anisotropic and multiband supercon-

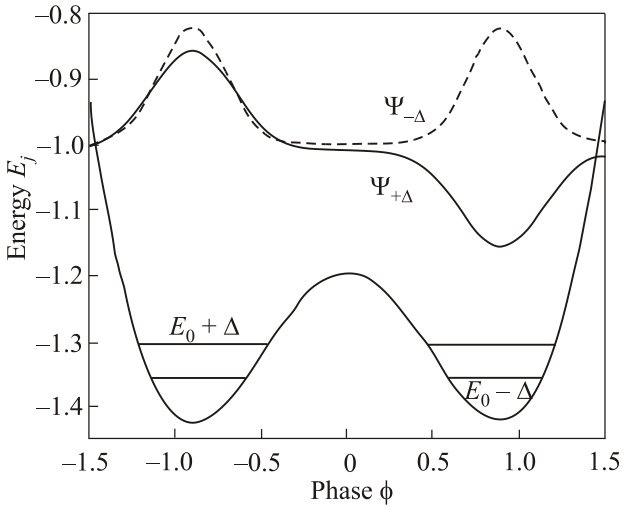

Fig. 33. Energy spectrum of silent qubit.

ductors show that in the general case CPR has anharmonic character. However, up to present time simple sinusoidal CPR was used to study the dynamics and ultimate performance of superconducting devices based on JJ. The main subject of this review is the investigation of dynamical properties of JJ with anharmonic CPR. Firstly, numerically calculated *I–V* characteristics of externally shunted JJ with anharmonic CPR were discussed. We conclude that the second harmonic in the CPR has a strong influence on the *I–V* curve of the JJ. Inclusion of anharmonicity parameters leads to an increase in the critical current and an enhancement of hysteresis in the *I–V* curves. We confirm that the shunt inductance in the range of $\beta_L < 15$ also affects the dynamics considerably.

Result of calculations of the plasma frequency of JJ with anharmonic CPR as function of anharmonicity parameter α was presented. Comparison of calculated plasma frequency with experimental data was conducted. Generalizing formulas for both harmonic and sub-harmonic Shapiro steps in the presence of nonzero junction capacitance and second harmonic in current-phase relation are discussed. Experimental results related to Shapiro steps in YBCO-based JJ are in good agreement with the theory. Simulations show that consideration of the second harmonic in CPR significantly changes the shape and stability properties of fluxon static distribution in long JJ.

We conclude that second harmonic in CPR has strong influence on the characteristics of phase qubits based on Josephson junctions, which operate at very low temperatures. In contrast to phase qubits, in the limit of charge qubits no considerable effects of anharmonicity are observed in the characteristic number of Cooper pair $\langle \hat{n} \rangle$ versus gate number n_g. It was observed that the influences of anharmonicity parameter α and the bias current i_b on the expectation value of supercurrent i_s in charge qubit are opposite. It was demonstrated that splitting of energy levels in phase qubit as well as energy gap in charge qubit reveals similar behavior with energy scale. Characteristics and operations of silent qubit using JJ with anharmonic CPR were also briefly discussed. Finally, we confirm that anharmonic current-phase relation must be taken into account in the experimental realizations of Josephson junction circuits and superconducting qubits.

Acknowledgements

I thank Professors F.M. Hashimzade, R.R. Guseinov, A. Gencer for the useful discussions, Dr. M. Canturk, Dr. A. Bozbey for collaboration and Dr. Erkan Bostanci for technical help. I am also grateful to the Abdus Salam ICTP for the hospitality during my stay as an associate member. This work was partly supported by the TUBITAK research grant No 111E191.

1. B.D. Josephson, *Phys. Lett*. **1**, 251 (1962).
2. J.M. Rowell, *Phys. Rev. Lett*. **11**, 200 (1963).
3. I.O. Kulik and I.K. Yanson, *Josephson Effect in Superconducting Tunneling Structures*, John Wiley & Sons, Incorporated (1972).
4. K.K. Likharev, *Dynamics of Josephson Junction and Circuits*, New York: Gorden Breach Publ. (1986).
5. K.K. Likharev, *Physica C* **482**, 6 (2012).
6. K.K. Likharev, *Usp. Phys. Nauk* **127**, 185 (1979).
7. K.K. Likharev, *Rev. Mod. Phys*. **51**, 101 (1979).
8. A.I. Buzdin, *Rev. Mod. Phys*. **77**, 935 (2005).
9. A.A. Golubov, M.Yu. Kupriyanov, and E. Il'ichev, *Rev. Mod. Phys*. **76**, 411 (2004).
10. C.C. Tsuei and J.R. Kirtley, *Rev. Mod. Phys*. **72**, 969 (2000).
11. J.R. Kirtley, *Rep. Prog. Phys*. **73**, 126501 (2010).
12. M. Sigrist and T.M. Rice, *Rev. Mod. Phys*. **67**, 503 (1995).
13. Yu.A. Kolesnichenko, A.N. Omelyanchouk, A.M. Zagoskin, *Fiz. Nizk. Temp*. **30**, 714 (2004) [*Low Temp. Phys*. **30**, 535 (2004)].
14. A. Barone and G. Paterno, *Physics and Application of the Josephson Effect*, Wiley-InterScience Publications, Canada (1982).
15. I. Askerzade, *Unconventional Superconductors: Anisotropy and Multiband Effects*, Springer (2012).
16. M. Sigrist and T.M. Rice, *J. Phys. Soc. Jpn*. **61**, 4283 (1992).
17. Y. Tanaka, *Phys. Rev. Lett*. **72**, 3871 (1994).
18. Y. Tanaka and S. Kashiwaya, *Phys. Rev. B* **56**, 897 (1997).
19. A.F. Andreev, *Sov. Phys. JETP* **19**, 1228 (1964).
20. L.N. Bulaevskii, V.V. Kuzii, and A.A. Sobyanin, *JETP Lett*. **25**, 290 (1977).
21. N.N. Bogolyubov, V.V. Tolmachev, and D.V. Shirkov, *New Method in Theory of Superconductivity*, Nauka, Moscow (1958).
22. V. Ambreokar and A. Baratoff, *Phys. Rev. Lett*. **10**, 486 (1963).
23. I.O. Kulik and A.N. Omel'yanchuk, *JETP Lett*. **21**, 96 (1975).
24. I.O. Kulik and A.N. Omel'yanchuk, *Fiz. Nizk. Temp*. **4**, 296 (1978) [*Sov. J. Low Temp. Phys*. **4**, 142 (1978)].
25. J. Nagamatsu, N. Nakagawa, T. Muranaka, Y. Zenitani, and J. Akimitsu, *Nature*, **410**, 63 (2001).
26. Y. Izyumov and E. Kurmaev, *High-T_c Superconductors Based on FeAs Compounds*, Springer (2010).
27. Y. Erin and A.N. Omelyanchouk, *Fiz. Nizk. Temp*. **36**, 1204 (2010) [*Low Temp. Phys.* **36**, 969 (2010)].
28. A.I. Buzdin, *JETP Lett*. **78**, 583 (2003).
29. A.I. Buzdin and M.Yu. Kupriyanov, *JETP Lett*. **53**, 321 (1991).
30. A.A. Golubov, M.Yu. Kupriyanov, and Ya.V. Fominov, *JETP Lett*. **75**, 190 (2002).
31. Y. Bazaliy, E. Demler, and S.-C. Zhang, *Phys. Rev. Lett*. **80**, 2917 (1998).
32. F.S. Bergeret, A.F. Volkov, and K.B. Efetov, *Rev. Mod. Phys*. **77**, 1321 (2006).

33. I.A. Garifullin, D.A. Tikhonov, N.N. Garif'yanov, L. Lazar, Yu.V. Goryunov, S.Ya. Khlebnikov, L.R. Tagirov, K. Westerholt, and H. Zabel, *Phys. Rev. B* **66**, R020505 (2002).
34. P. Komissinskiy, G.A. Ovsyannikov, I.V. Borisenko, Yu.V. Kislinskii, K.Y. Constantinian, A.V. Zaitsev, and D. Winkler, *Phys. Rev. Lett.* **99**, 017004 (2007).
35. L.R. Gor'kov and V.Z. Kresin, *Physica C* **367**,103 (2002).
36. A.J. Dahm, A. Denenstein, T.F. Finnegan, D.N. Langenberg, and D.J. Scalapino, *Phys. Rev. Lett.* **20**, 859 (1968).
37. N. Grønbech-Jensen, M.G. Castellano, F. Chiarello, M. Cirillo, C. Cosmelli, L.V. Filippenko, R. Russo, and G. Torrioli, *Phys. Rev. Lett.* **93**, 107002 (2004).
38. E. Il'ichev, M. Grajcar, R. Hlubina, R.P.J. IJsselsteijn, H.E. Hoenig, H.-G. Meyer, A. Golubov, M.H.S. Amin, A.M. Zagoskin, A.N. Omelyanchouk, and M.Yu. Kupriyanov, *Phys. Rev. Lett.* **86**, 5369 (2001).
39. E. Il'ichev, V. Zakosarenko, L. Fritzsch, R. Stolz, H.E. Hoenig, H.-G. Meyer, M. Gotz, A.B. Zorin, V.V. Khanin, A.B. Pavolotsky, and J. Niemeyer, *Rev. Sci. Instrum*. **72**, 1882 (2001).
40. A.H. Silver and J.E. Zimmerman, *Phys. Rev*. **157**, 317 (1967).
41. R. Rifkin and B.S. Deaver, *Phys. Rev. B* **13**, 3894 (1976).
42. E. Il'ichev, H.E. Hoenig, H.-G. Meyer, A.B. Zorin, V.V. Khanin, M. Götz, A.B. Pavolotsky, and J. Niemeyer, *Physica C* **352**, 141 (2001).
43. E. Il'ichev, V. Zakosarenko, R.P.J. IJsselsteijn, H.E. Hoenig, H.-G. Meyer, M.V. Fistul, and P. Müller, *Phys. Rev. B* **59**, 11502 (1999).
44. T. Bauch, F. Lombardi, F. Tafuri, A. Barone, G. Rotoli, P. Delsing, and T. Claeson, *Phys. Rev. Lett.* **94**, 087003 (2005).
45. G.A. Ovsyannikov and K.I. Konstantinyan, *Fiz. Nizk. Temp*. **38**, 423 (2012) [*Low Temp. Phys*. **38**, 333 (2012)].
46. C. Chialvo *et al*., *cond-mart, arxiv1005.2630.*
47. Annica M. Black-Schaffer and Jacob Linder, *Phys. Rev. B* **82**, 184522 (2010).
48. L. Fu, C.L. Kane, and E.J. Mele, *Phys. Rev. Lett*. **98**, 106803 (2007).
49. M.Z. Hasan and C.L. Kane, *Rev. Mod. Phys*. **82**, 3045 (2010).
50. Xiao-Liang Qi and Shou-Cheng Zhang, *Rev. Mod. Phys*. **83**, 1057 (2011).
51. L. Fu and C.L. Kane, *Phys. Rev. B* **79**,161408 (2009).
52. P.A. Ioselevich and M.V. Feigel'man, *Phys. Rev. Lett*. **106**, 077003 (2011).
53. J.R. Williams, A.J. Bestwick, P. Gallagher, Seung Sae Hong, Y. Cui, Andrew S. Bleich, J.G. Analytis, I.R. Fisher, and D. Goldhaber–Gordon, *Phys. Rev. Lett*. **109**, 056803 (2012).
54. A. Zubkov, M. Kupriyanov, and V. Semenov, *Fiz. Nizk. Temp*. **7**, 1365 (1981) [*Sov. J. Low Temp. Phys*. **7**, 661 (1981)].
55. C.B. Whan and C.J. Lobb, *J. Appl. Phys*. **77**, 382 (1995).
56. A.B. Cawthorne, C.B. Whan, and C.J. Lobb, *J. Appl. Phys*. **84**, 1126 (1998).
57. M. Canturk and I.N. Askerzade, *IEEE Appl. Supercond*. **22**, 1400106 (2012).
58. E. Goldobin, D. Koelle, R. Kleiner, and A. Buzdin, *Phys. Rev. B* **76**, 224523 (2007).
59. N. Calander, T. Claeson, and S. Rudner, *Appl. Phys. Lett*. **39**, 504 (1981).
60. I.N. Askerzade and V.K. Kornev, *Radiotekh. Elekt*. **39**, 869 (1994).
61. I.N. Askerzade, *Techn. Phys*. **48**, 1496 (2003).
62. M. Abramovitz and A. Stegun, *Handbook on Math. Functions*, Dover, New York (1972).
63. I.N. Askerzade, *Techn. Phys. Lett.* **31**, 622 (2005).
64. S. Shapiro, *Phys. Rev. Lett*. **11**, 80 (1963).
65. D. Cassel, G. Pickartz, M. Siegel, E. Goldobin, H.H. Kohlstedt, A. Brinkman, A.A. Golubov, M.Yu. Kupriyanov, and H. Rogalla, *Physica C* **450**, 76 (2001).
66. V.K. Kornev, T.Y. Karminskaya, Y.V. Kislinskii, P.V. Komissinki, K.Y. Constantinian, and G.A. Ovsyannikov, *Physica C* **435**, 27 (2006).
67. P.V. Komissinski, K.I. Constantinian, Yu. Kislinskii, and G.A. Ovsyannikov, *Fiz. Nizk. Temp*. **30**, 795 (2004) [*Low Temp. Phys.* **30**, 599 (2004)].
68. Y. Kislinskii, P. Komissinski, K. Constantinian, G. Ovsyannikov, T. Karminskaya, I. Soloviev, and V. Kornev, *JETP* **101**, 494 (2005).
69. R. Kleiner, A.S. Katz, A.G. Sun, R. Summer, D.A. Gajewski, S.H. Han, S.I. Woods, E. Dantsker, B. Chen, K. Char, M.B. Maple, R.C. Dynes, and John Clarke, *Phys. Rev. Lett.* **76**, 2161 (1996).
70. P.Kh. Atanasova, T.L. Boyadjiev, Yu.M. Shukrinov, and E.V. Zemlyanaya, *Proc. FDM10*, Lozenetz, Bulgaria (2010).
71. P.Kh. Atanasova, T.L. Boyadjiev, Yu.M. Shukrinov, and E.V. Zemlyanaya, *J. Phys., Conf. Ser*. **248**, 012044 (2010).
72. P.Kh. Atanasova, T.L. Boyadjiev, Yu.M. Shukrinov, and E.V. Zemlyanaya, *Lecture Notes Computer Science* **6046**, 347 (2011).
73. Y.S. Galperin and A.T. Filippov, *Sov. Phys. JETP* **59**, 89 (1984).
74. M.A. Nielsen and I.L. Chuang, *Quantum Computation and Quantum Information*, Cambridge, University Press (2000).
75. K.A. Valiev, *Phys. Usp*. **48**, 1 (2008).
76. T. Bauch, T. Lindstro, F. Tafuri, G. Rotoli, P. Delsing, T. Claeson, and F. Lombardi, *Science* **311**, 57 (2006).
77. M.H.S. Amin, A.Yu. Smirnov, A.M. Zagoskin, T. Lindström, S.A. Charlebois, T. Claeson, and A.Ya. Tzalenchuk, *Phys. Rev. B* **71**, 064516 (2005).
78. N. Klenov, V. Kornev, and N. Pedersen, *Physica C* **435**, 114 (2006).
79. N. Klenov, V. Kornev, A. Vedyayev, N. Ryzhanova, N. Pugach, T. Rumyantseva, *J. Phys., Conf. Ser*. **97**, 012037 (2008).
80. N. Klenov, N. Pugach, A. Sharafiev, S. Bakursky, and V. Kornev, *Phys. Solid State* **52**, 2246 (2010).
81. M. Canturk, E. Kurt, and I.N. Askerzade, *Int. J. Comput. Math. Elect. Electron. Eng*. **30**, 775 (2011).
82. M. Canturk and I.N. Askerzade, *IEEE Appl. Supercond*. **23**, 3541 (2011).

83. G. Wendin and V.S. Shumeiko, *Fiz. Nizk. Temp*. **33**, 957 (2007) [*Low Temp.Phys.* **33**, 724 (2007)].
84. T. Yamashita, K. Tanikawa, S. Takahashi, and S. Maekawa, *Phys. Rev. Lett.* **95**, 097001 (2005).
85. N. Nakamura, Y.A. Pashkin, and J.S. Tsai, *Nature* **398**, No. 6730, 786 (1999).
86. K.K. Likharev and A. Zorin, *J. Low Temp. Phys.* **59**, 347 (1985).
87. A. Bjorek and G. Golub, *SIAM Rev*. **19**, 5 (1977).
88. D. Evans and S. Okolie, *Comput. Math. Appl*. **8**, 175 (1982).
89. I.N. Askerzade, *Tech. Phys*. **56**, 744 (2011).
90. J. Zaiman, *Principles of the Solids*, Cambridge Univ. Press, UK (1995).
91. V. Bouchiat, D. Vion, P. Joyez, D. Esteve, C. Urbina, and M.H. Devoret, *Appl. Supercond*. **6**, 491 (1998).